AGU PUBLICATIONS

JGR

Journal of Geophysical Research: Atmospheres

RESEARCH ARTICLE

10.1002/2014JD022932

Key Points:

- Cloud phase intermodel differences are very large
- Prognostic cloud phase scheme is necessary to reproduce realistic cloud phase
- These results could lead to an improvement of the next generation of GCMs

Supporting Information:

- Figures S1–S3

Correspondence to:
G. Cesana,
Gregory.v.cesana@jpl.nasa.gov

Citation:
Cesana, G., D. E. Waliser, X. Jiang, and J.-L. F. Li (2015), Multimodel evaluation of cloud phase transition using satellite and reanalysis data, *J. Geophys. Res. Atmos.*, *120*, 7871–7892, doi:10.1002/2014JD022932.

Received 3 DEC 2014
Accepted 24 JUN 2015

Multimodel evaluation of cloud phase transition using satellite and reanalysis data

G. Cesana[1], D. E. Waliser[1], X. Jiang[1,2], and J.-L. F. Li[1]

[1]Jet Propulsion Laboratory, California Institute of Technology, Pasadena, California, USA, [2]Joint Institute for Regional Earth System Science and Engineering, University of California, Los Angeles, California, USA

Abstract We take advantage of climate simulations from two multimodel experiments to characterize and evaluate the cloud phase partitioning in 16 general circulation models (GCMs), specifically the vertical structure of the transition between liquid and ice in clouds. We base our analysis on the ratio of ice condensates to the total condensates (phase ratio, PR). Its transition at 90% (PR90) and its links with other relevant variables are evaluated using the GCM-Oriented Cloud-Aerosol Lidar and Infrared Pathfinder Satellite Observation Cloud Product climatology, reanalysis data, and other satellite observations. In 13 of 16 models, the PR90 transition height occurs too low (6 km to 8.4 km) and at temperatures too warm (−13.9°C to −32.5°C) compared to observations (8.6 km, −33.7°C); features consistent with a lack of supercooled liquid with respect to ice above 6.5 km. However, this bias would be slightly reduced by using the lidar simulator. In convective regimes (more humid air and precipitation), the observed cloud phase transition occurs at a warmer temperature than for subsidence regimes (less humid air and precipitation). Only few models manage to roughly replicate the observed correlations with humidity (5/16), vertical velocity (5/16), and precipitation (4/16); 3/16 perform well for all these parameters (MPI-ESM, NCAR-CAM5, and NCHU). Using an observation-based Clausius-Clapeyron phase diagram, we illustrate that the Bergeron-Findeisen process is a necessary condition for models to represent the observed features. Finally, the best models are those that include more complex microphysics.

1. Introduction

In the context of global warming, a good representation of clouds by climate models is a key feature needed to accurately represent cloud-climate feedbacks in the present and future climate. The ubiquitous presence of clouds within the troposphere (global total cloud frequency about 70% [*Stubenrauch et al.*, 2013]) strongly characterizes the radiative balance of the Earth-atmosphere system [*Kiehl and Trenberth*, 1997; *Wielicki et al.*, 1996]. For a given water content, the optical depth of a liquid cloud is higher than the one of an ice cloud [*Rogers and Yau*, 1989], resulting in very different radiative effects. When liquid droplets occur in conjunction with ice crystals in clouds, hereafter referred as mixed-phase cloud, the cloud radiative forcing at the surface is even more difficult to model than for the non-mixed-phase clouds. Mixed-phase clouds may lead to opposite effects on surface temperature depending on the thermodynamic conditions: a cooling in middle latitudes [*Hogan et al.*, 2003; *Sun and Shine*, 1994] or a warming in the Arctic [*Shupe and Intrieri*, 2004; *Zuidema et al.*, 2005].

At temperatures above the freezing level, cloud can only be composed of liquid droplets, whereas below the homogeneous freezing temperature (around −40°C [*Pruppacher and Klett*, 1997]), all the condensed water is frozen. In between, liquid and ice particles can coexist in mixed-phase clouds typically for a few hours [*Korolev et al.*, 2003], but sometimes longer, for instance in Arctic [e.g., *de Boer et al.*, 2009]. As the saturation vapor pressure is lower with respect to ice than that to liquid, ice crystals eventually form at the expense of liquid droplets by vapor deposition, modifying the cloud phase partitioning, through the so-called Bergeron-Findeisen (BF) process [*Bergeron*, 1935; *Findeisen*, 1938]. The growth of cloud particles through collection and their autoconversion to form rain and snow depend on the cloud phase as well [*Tao and Simpson*, 1993; *Tao*, 2003].

The parameterization of the cloud phase has become of particular interest since numerous studies have shown its impact on the climate sensitivity of general circulation models (GCMs) [e.g., *Li and Le Treut*, 1992; *Gregory and Morris*, 1996; *Doutriaux-Boucher and Quaas*, 2004; *Cesana et al.*, 2012]. Recent studies took advantage of the Cloud-Aerosol Lidar and Infrared Pathfinder Satellite Observation (CALIPSO) [*Winker et al.*, 2010] cloud phase observations to characterize and underscore GCM cloud and radiation shortcomings. For example, *Cheng et al*. [2012] showed that a modification of the cloud phase partitioning in a GCM, based on CALIPSO level 2 observations, could generate positive or negative feedbacks in the cloud fraction, impacting humidity and temperature profiles. *Komurcu et al*. [2014] showed that employing the same ice nucleation parameterization in four GCMs was not sufficient for matching to the cloud top supercooled liquid fraction of CALIPSO level 2 observations and to reduce the cloud phase GCMs' spread. However, while these two studies improved our understanding of modeled cloud phase performance, they only utilized a few GCMs and neither compared the simulations with GCM-oriented observation products nor used simulators. Based on the discussion above, improving our knowledge of the cloud phase characteristics among the multitude of GCMs via observations well suited for model evaluation is a needed element to reduce cloud-climate feedback uncertainties.

The cloud phase transition, along with the BF process, and their related mechanisms (e.g., condensation types and autoconversion) and variables (e.g., particle number and size and particle fall speed) happen at spatial-temporal (microphysical) scales too small to be resolved by climate models. Until recently, GCMs typically separated liquid from ice using a simple relation between the ratio of the ice mass to the total condensate based on the temperature measurements from aircraft campaigns [*Bower et al*., 1996; *Cober et al*., 2001; *Feigelson*, 1978]. These in situ measurements show different relations depending on the type of clouds that were probed, and hence, are not readily adapted to the GCMs grid scales. Recent generations of GCMs have begun to include more complex microphysics in their cloud scheme (e.g., prognostic ice and liquid water content, heterogeneous freezing, contact freezing, riming, accretion, and BF process). Yet the vertical distribution of the water content continues to be challenging even for models including more complex cloud phase scheme [e.g., *Waliser et al*., 2009; *Chen et al*., 2011; *Li et al*., 2012].

The large variability of the modeled liquid and ice water content (see Figures S1 and S2 in the supporting information) combined with the lack of observational constraints make it difficult to clearly diagnose and propose solutions for cloud phase biases in the models. A way to bridge the gap is to investigate the Mass Phase Ratio (MPR), which is the ratio of the ice mass (IWC) to the total (IWC + LWC) mass of the condensed water. No matter the assumptions made to compute the LWC and IWC, the MPR allows a meaningful and easy comparison of all models by taking into account the contribution of both liquid and ice water phases in cloud, regardless of the cloud fraction [e.g., *Tsushima et al*., 2006; *Cesana and Chepfer*, 2013]. Besides, the MPR has been often used to parameterize GCMs [e.g., *Smith*, 1990; *Tiedtke*, 1993]. While a robust observed reference for MPR is yet to exist, the recent release of the GCM-Oriented CALIPSO Cloud Product (CALIPSO-GOCCP) [*Cesana and Chepfer*, 2013] makes it possible to estimate the frequency of occurrence of liquid and ice clouds and compute the Frequency Phase Ratio (FPR), which is the ratio of the ice cloud occurrence to the total cloud occurrence (liquid + ice). Unfortunately, climate models do not simulate ice and liquid cloud occurrences without the use of lidar simulaltor. However, under specific conditions (discussed further in section 2.3), the observed FPR can be effectively used to assess the modeled MPR, without using a simulator. In short, CALIPSO-GOCCP distinguishes liquid clouds from ice clouds, over several vertical layers, with a spatial-temporal sampling adapted to GCMs—including global coverage—above reflective surfaces and continent, for more than 7 years. This product offers new opportunity for climate modeling teams to evaluate their cloud phase scheme.

In this paper, we will take advantage of recent climate simulations from two multimodel experiments to characterize and compare the cloud phase representations in 16 models: (i) the joint multimodel project organized by the Global Energy and Water Cycle Exchange Project's Atmosphere System Study (GASS) Program, the Year of Tropical Convection (YoTC) activity, and Madden-Julian Oscillation Task Force (GASS-YoTC/MJOTF) [*Petch et al*., 2011; *Jiang et al*., 2015] and (ii) the Atmospheric Model Intercomparison Project (AMIP) [*Gates*, 1992] of the Coupled Model Intercomparison Project Phase 5 (CMIP5) [*Taylor et al*., 2012]. A particular emphasis will be put on the vertical structure of the transition between liquid and ice in clouds, and how this may be systematically related to the underlying parameterizations. We will also take advantage of the new cloud phase climatology based on the CALIPSO-GOCCP data set, designed for GCMs evaluation, to address the challenge of evaluating a specific aspect of the modeled cloud phase: the height and temperature of the transition between mixed-phase clouds and ice clouds. The 16 models, CALIPSO-GOCCP observations, and the methods to compare the two will be introduced in section 2. Then, the links between the cloud phase and height, temperature, relative humidity, vertical wind speed, and precipitation will be discussed in section 3.

Table 1. Overview of the 16 GCMs[a]

Model	Experiment	Coupled/AGCM	Cloud Phase	Reference
BCCAGCM2.1*	YoTC-MJOTF	AGCM	T-dependent; linear between −10°C and −40°C	*Wu et al.* [2010]
CanCM4	YoTC-MJOTF	Coupled	Prognostic liquid and ice; complex microphysics	*von Salzen et al.* [2013]
CCSM4*	CMIP5-AMIP	AGCM	T-dependent; linear between −10°C and −40°C	*Neale et al.* [2010a]
CNRM-CM5*	CMIP5-AMIP	AGCM	T-dependent; $f = (1 - \exp(-(T - T_t)^2/(2^*dT^2))$ $dT = 11.82$ K and $T_t = 273.16$ K	*Voldoire et al.* [2011]
EC-earth3$^{*,\Delta}$	YoTC-MJOTF	AGCM	T-dependent; $f = (T - T_{ice}/T_0 - T_{ice})^2$ $T_0 = 273.16$ K and $T_{ice} = 250.16$ K; BF	IFS cycle 36r1 (part4)
GEOS5-AGCM$^{*,\Delta}$	YoTC-MJOTF	AGCM	T dependent; linear between 0°C and −38°C; BF	*Molod et al.* [2012]
GFDL-CM3$^{\Delta}$	CMIP5-AMIP	AGCM	Prognostic liquid and ice; Mixed between 0°C and −40°C; liquid droplets form first; BF	*Donner et al.* [2011]
GISS/ModelE$^{*,\Delta}$	YoTC-MJOTF	AGCM	T dependent; $f = 1 - \exp[-(T_0 - T/15)^2]$; $T_0 = -4$°C over ocean and −10°C over land; BF	*Schmidt et al.* [2006]
HadGEM2-A$^{\Delta}$	CMIP5-AMIP	AGCM	Prognostic liquid and ice; complex microphysics; BF	*Martin et al.* [2011]
IPSL-CM5A-LR*	CMIP5-AMIP	AGCM	T dependent; linear between 0°C and −15°C	*Hourdin et al.* [2013]
ISU-GCM*	YoTC-MJOTF	AGCM	T dependent; linear between −10°C and −40°C	*Deng and Wu* [2010]
MIROC5$^{\Delta}$	CMIP5-AMIP	AGCM	Prognostic liquid and ice; complex microphysics; BF;	*Watanabe* [2010]
MPI-ESM	YoTC-MJOTF	Coupled	Prognostic liquid and ice; mixed between 0°C and −35°C; different over land and ocean; complex microphysics	*Stevens et al.* [2013]
MRI-AGCM$^{*,\Delta}$	YoTC-MJOTF	AGCM	2 T-dependent [*Tiedtke*, 1993; *Smith*, 1990] 1 Prognostic liquid and ice (MRI-TMBC); complex microphysic; BF	*Yukimoto et al.* [2012]
NCAR-CAM5$^{\Delta}$	YoTC-MJOTF	AGCM	Prognostic liquid and ice; complex microphysics; BF	*Neale et al.* [2010b]
NCHU-ECHAM5-SIT	YoTC-MJOTF	Coupled	Same as MPI	*Tsuang et al.* [2009]

[a] The stars (*) indicate T-dependent models (diagnostic cloud phase) and the delta (Δ) indicate models including Bergeron-Findeisen process (BF).

In section 4, we will characterize the BF process, which strongly impacts the cloud phase partitioning, via the Clausius-Clapeyron (C-C) phase diagram, using modeled and observed data sets not averaged in time and space. Finally, we will summarize the results in section 5.

2. Data and Method

2.1. Modeled Data

We analyze outputs from 16 climate models, which are listed in Table 1 with the corresponding references. We selected 10 model outputs from the climate simulation component of the GASS-YoTC/MJOTF multimodel experiment [*Jiang et al.*, 2015]. The GASS and YoTC/MJOTF partnership gathers complementary expertise to advance our knowledge of the physical processes affecting vertical structure and tropical climate/variability. The climate simulations from this project (one of three experimental components) required outputting the requested variables every 6 h, with a spatial resolution of 2.5 by 2.5°, over 22 pressure levels from 1000 hPa to 50 hPa and for 20 years. Although the multimodel climatological component contains 27 models, only 10 of them met the variable requirements for our analysis: LWC, IWC, temperature, relative humidity, and vertical velocity. All the selected GASS-YoTC/MJOTF simulations were forced by the observed sea surface temperature (SST) except the Max Planck Institute Earth System Model (MPI-ESM), the Canadian fourth generation of Coupled global climate Model (CanCM4), and the National Chung Hsing University model (NCHU), which have coupled oceans. We downloaded six other model simulations from the Earth System Grid Federation website (http://esg-datanode.jpl.nasa.gov/esgf-web-fe/). These outputs have been submitted by the modeling centers within the framework of the CMIP5-AMIP experiment (using prescribed SST) for the Intergovernmental Panel on Climate Change Fifth Assessment Report [*Stocker et al.*, 2013]. For a matter of consistency of the spatial-temporal resolution of the models' outputs, the CMIP5-AMIP daily files have been linearly interpolated onto the YoTC-MJOTF vertical and horizontal grid, and the GASS-YoTC/MJOTF 6-hourly files have been averaged to daily values. Differences between the 6-hourly metric and the daily metric—used later on (MPR90, section 2.3)—are negligible relative to the model-observation differences and do not influence the results of the study (not shown). The daily averaging also ensures better consistency with the observed metric (FPR, section 2.3, computed from daily files). Only 1 year of simulation is used in this comparative study for two reasons. First, the variability of zonally averaged MPR on interannual timescale is negligible (Appendix A). Second, daily sampling over 1 year simulation constitutes a statistically representative data set.

The different microphysics schemes of the models employed in this study are varied and complex, to describe all of them is beyond the scope of this paper. Thus, we only include the most common and important features related to cloud phase in Table 1. In GCMs, the thermodynamic phase of cloud particles can be treated prognostically or diagnostically. Overall, 9 of the 16 models separate the liquid and ice water content diagnostically, as a function of temperature (models marked with a star, first column of Table 1), hereafter called *T*-dependent models. Among these nine *T*-dependent models, five—referred as "strictly *T* dependent"—strictly use the temperature for the cloud phase partitioning. The seven other models (without star) prognose the ice and liquid water content depending on particle number, cloud condensation nuclei, total water content, etc. These models also take into account complex microphysics processes such as homogenous and heterogeneous nucleation, evaporation, deposition, contact freezing, and other processes induced by precipitation (e.g., autoconversion) [e.g., *Neale et al.*, 2010b; *Stevens et al.*, 2013]. However, they may use the temperature to split ice and liquid condensates in specific cases—for example, the shallow cumulus detrainment in National Center for Atmospheric Research-Community Atmospheric Model version 5 (NCAR-CAM5). Finally, 8 of the 16 models (marked with a triangle, first column of Table 1; including three with *T*-dependent schemes) take into account the BF mechanism, which has a large impact on mixed-phase clouds.

In section 4, we use output from eight models that participated in component 2 of the GASS-YoTC/MJOTF experiment [*Petch et al.*, 2011]. This hindcast component aims to study two successive MJO events during boreal winter 2009–2010 with highly detailed outputs. For this reason, these outputs have high (i.e., every time step) temporal resolution (typically around 15 min) for two time periods of 20 days (from 20 October 2009 to 10 November 2009 and from 20 December 2009 to 10 January 2010) along with the model's original spatial resolution. They are limited to a particular near-equatorial Indian Ocean/Western Pacific Ocean domain (10°S–10°N and 60°E–160°E).

2.2. The GCM-Oriented CALIPSO Cloud Product (CALIPSO-GOCCP)

Within the framework of Cloud Feedback Model Intercomparisoin Project (CFMIP) [*Bony et al.*, 2011], the Laboratoire de Météorologie Dynamique (LMD) has designed CALIPSO-GOCCP [*Chepfer et al.*, 2010] to facilitate the evaluation of clouds in climate models [e.g., *Cesana and Chepfer*, 2012] with the joint use of the CALIPSO simulator [*Chepfer et al.*, 2008]. CALIPSO-GOCCP is based on level 1 measurements of the CALIPSO satellite, which flies in a 705 km Sun-synchronous polar orbit, crossing the equator at 1:30 A.M. and 1:30 P.M. local solar time. CALIPSO-GOCCP utilizes the ratio of the total attenuated backscattered signal to the molecular attenuated backscattered signal (in the presence of molecules only) to compute along-track cloud mask profiles, with spacing every 333 m, and with 480 m vertical resolution. The polarization-sensitive CALIPSO lidar allows the discrimination of liquid droplets from ice crystals by comparing the polarization of the backscattered signal with the emitted signal. For spherical droplets, the backscattered polarization signal remains quite unchanged, whereas nonspherical ice crystals introduce additional cross polarization in the signal. Based on these optical properties, *Cesana and Chepfer* [2013] built a discrimination threshold to separate ice-dominated clouds and liquid-dominated clouds in CALIPSO-GOCCP. In less than 1% of the cases, a temperature criterion is applied that prevents liquid clouds to be diagnosed as ice clouds for temperature above the freezing level and vice versa for temperatures colder than -40°C (homogeneous freezing of supercooled liquid droplets). The temperature profiles are included in the level1 CALIPSO files and come from the Modern-Era Retrospective Analysis for Research and Applications (MERRA) reanalysis [*Rienecker et al.*, 2011]. Then, they compute the frequency of occurrence of ice clouds (Ice Cloud Fraction, ICF) and liquid clouds (Liquid Cloud Fraction, LCF) in each grid cell [see *Cesana and Chepfer*, 2013, Appendix A2]. Finally, they define the Frequency Phase Ratio (FPR) as the ratio of ice clouds to total clouds (ice + liquid).

The CALIPSO-GOCCP cloud phase product (together with two other CALIPSO products) has been compared with in situ measurements by G. Cesana et al. (Evaluation of three CALIPSO cloud phase products using in-situ airborne measurements, submitted to *Journal of Atmospheric and Oceanic Technology*, 2015). The presence of substantial supercooled liquid below -30°C was found in all CALIPSO products, in agreement with previous in situ and ground-based measurements [*Korolev et al.*, 2003; *Naud et al.*, 2010]. However, they showed that the CALIPSO cloud phase retrievals (including CALIPSO-GOCCP) over a 480 m pixel are dominated by the signal of the top cloudy layer. For this reason, CALIPSO-GOCCP observations may overestimate the liquid-only and ice-only cloud occurrences, depending on the cloud top phase. Besides, due to its attenuation, the lidar beam cannot go through optically thick clouds (optical depth > 3) and may not detect some ice crystals underneath the optically thick stratocumulus clouds (most likely falling particles). This may potentially lead to a slight underestimation of ice clouds in the lowest levels at midlatitudes and in polar regions.

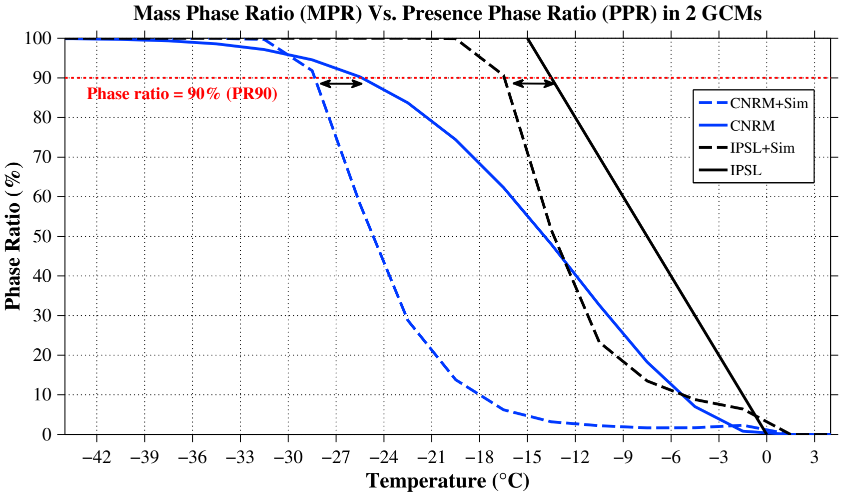

Figure 1. Relation between cloud phase ratio (PR; *y* axis, %) and temperature (*x* axis, °C) simulated by CNRM (blue solid line) and IPSL (black solid line) models (Mass Phase Ratio, MPR) and simulated by CNRM (blue dashed line) and IPSL (black dashed line) models through the lidar simulator (Presence Phase Ratio, PPR). The red dotted line represents the PR90 transition level. The black arrows help to locate the differences between the MPR and the PPR when PR value is 90%, for both models.

2.3. Method

Satellites do not measure directly the quantity simulated by climate models. Consequently, assumptions are made to retrieve the geophysical variables, which may lead to substantial biases [e.g., *Stephens and Kummerow*, 2007; *Stubenrauch et al*., 2013]. Besides, the instruments on board satellites are subject to physical limitations that may not allow detecting all the features under all circumstances (e.g., lidar attenuation [*Chepfer et al*., 2010]; partly cloudy pixels [*Pincus et al*., 2012]), nor does their sampling match the GCM spatial-temporal output characteristics (e.g., heliosynchroneous orbit of A-Train). The "simulator" approach [e.g., *Cesana et al*., 2012; *Klein and Jakob*, 1999; *Marchand et al*., 2009] is a way to exploit satellite observations in model evaluation. Since no simulators were used in the GASS-YoTC/MJOTF experiments, we have developed and applied a method that allows comparing observations directly with the models.

First, we ensure that simulations and observations are comparable. Here we use two slightly different quantities: the modeled MPR versus the observed FPR. The FPR is a measure of how frequent an ice cloud is present with respect to liquid and ice clouds in a given grid cell, as opposed to the MPR that denotes whether liquid or ice dominates with respect to the total condensate mass. Differences between the FPR and MPR have already been pointed out in the literature: for example, by combining CALIPSO cloud phase standard products with the ice and liquid water path from Moderate Resolution Imaging Spectroradiometer (MODIS) [see *Hu et al*., 2010, see Figure 6f], or based on the use of the lidar simulator on Institut Pierre-Simon Laplace (IPSL) model [see *Cesana and Chepfer*, 2013, Figure 11b]. However, in both studies cited above, these differences substantially decrease as the FPR and MPR values increase and get close to 100%. Figure 1 shows the MPR of the IPSL (black solid line) and Centre National de Recherches Météorologiques (CNRM) (blue solid line) models along with their respective FPR (colored dotted lines) obtained by using the lidar simulator. This figure shows what would be the PR if it were retrieved using a virtual lidar overflying the modeled atmosphere. For both models, the use of the lidar simulator introduced an underestimation of the PR at the same temperature because the lidar-like cloud phase is mostly dominated by the presence of liquid in clouds, especially for liquid-topped clouds (cf. last paragraph of section 2.2). Thus, the FPR lines are shifted to colder temperatures compared to MPR lines, which is referred as the "lidar effect" on the PR. For both models, the lidar effect on the MPR (cold bias) is the largest for low PR values and is significantly reduced near high PR values (see black arrows at 90%, Figure 1). For example, the cold bias in the transition temperatures is larger at PR = 40% (−12°C and −6°C for CNRM and IPSL, respectively) than at PR = 90% (around −3°C in both models). Consequently, we focus the model evaluation against the "observed" values on PRs above 90%, contrary to previous studies that considered the full range of PRs [e.g., *Komurcu et al*., 2014]. The advantages of this threshold are twofold: (i) this affords the means to perform a consistent comparison between MPR with FPR—while no simulator is used—and (ii) this gives information

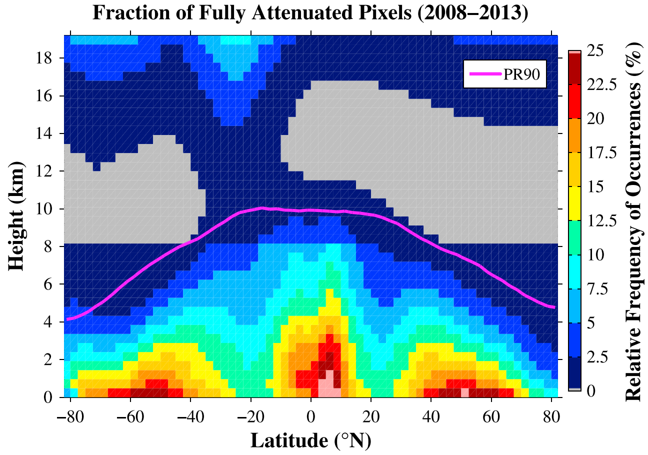

Figure 2. Annual and zonal mean (*x* axis, °N) profiles (*y* axis, km) of fully attenuated fraction (%) observed by CALIPSO-GOCCP (January 2008 to December 2013) [*Chepfer et al*., 2010]. The magenta line corresponds to the 90% phase ratio isocontour (PR90). The PR90 is located above the highest concentration of fully attenuated pixels, meaning that the PR90 zonal mean is only weakly affected by the lidar attenuation. Note that the substantial fully attenuated fractions above 16 km are due to noise in the high troposphere where the signal is highly sensitive to noise.

about heights and temperatures at which no more liquid is simulated by GCMs, which is a key parameter to compute radiative response of clouds [e.g., *Forbes and Ahlgrimm*, 2014].

Second, we take into account the observation limitations. The main bias of CALIPSO lies in attenuation of the laser beam that prevents the lidar signal from passing through clouds with an optical depth higher than three (typically the dense liquid clouds or convective anvil clouds). However, the high values of MPR and FPR occur in the high troposphere (typically above 6.5 km) where the temperature drops below −30°C. At that height, lidar observations are hardly affected by lidar attenuation, as illustrated in Figure 2. The full attenuation of the lidar happens less than 2.5% of the time when FPR is near 90% (FPR90, magenta line). Besides, the 90% value allows reducing the use of the temperature criterion of −40°C in observations, making the diagnosis less dependent on the temperature. And finally, the observed pixels near FPR90 are less affected by noise than at FPR100 [*Cesana and Chepfer*, 2013] (see Figures 2 and 3). Using FPR90 therefore significantly reduces the observation biases.

Further analysis on the difference between the FPR and MPR at 90% (FPR90 and MPR90) has been performed using the IPSL model and the simulator (not shown). We found a zonal mean temperature difference of −3.05°C—consistent with Figure 1—and a zonal mean height difference of +680 m between the FPR90 and the MPR90, which is much smaller than most model-observation differences found in our study (cf. section 3). These differences do not vary significantly in time and space (not shown). At 50%, differences increased to −6.3°C and +1.25 km (between 40°S/N), highlighting the need to stay in the high FPRs/MPRs to limit biases in the comparison. Also, a sensitivity study comparing CALIPSO-GOCCP FPR and the 16-modeled MPRs at 50% leads to similar qualitative results and conclusions than the ones at 90% (see Figure S3 in the supporting information and compare to section 5 and Figure 12). Choosing 90% FPR/MPR value does not change the overall conclusions while permits a quantitative evaluation of the models. Therefore, the CALIPSO-GOCCP temperature (or height for similar reasons) at FPR90 is a relevant metric that can be consistently used to assess the cloud phase transition in climate models in absence of simulator. For a matter of simplicity, we will refer to PR and PR90 for both models and observations instead of FPR/MPR and FPR90/MPR90, in the next sections.

Third, we used CALIPSO-GOCCP daily mean data with 2.5 by 2.5° horizontal grid averaging, which is the same as the two GCMs experiments, to reduce the uncertainties related to the spatial-temporal sampling.

In this paper, we also illustrate and discuss model intercomparison of the MPRs across full range of PRs, as the simulated MPR values by the models can be directly compared, and significant information on the varied model behavior relative to their parameterization is evident from such a comparison.

3. Results

3.1. Height

Figure 3 shows the zonal average of PR profiles simulated by 16 GCMs (listed alphabetically; *T*-dependent models marked with a star and models including the BF process marked with a delta) and observed by CALIPSO-GOCCP on the bottom right corner (2008 to 2013). The light blue shading represents a PR of 0%,

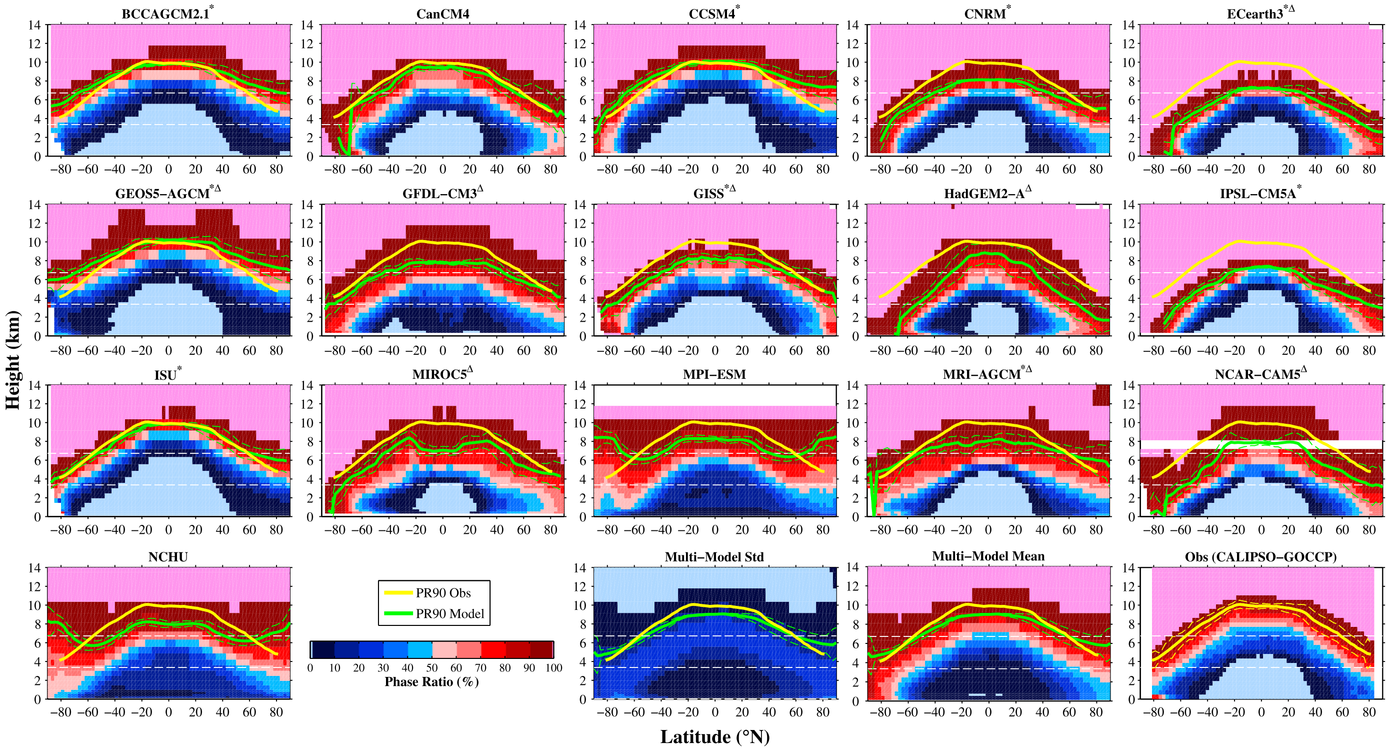

Figure 3. Annual and zonal mean (*x* axis, °N) profiles (*y* axis, km) of cloud fraction phase ratio (PR, %) simulated by 16 GCMs (Mass Phase Ratio, MPR) and observed by CALIPSO-GOCCP (Presence Phase Ratio, PPR; January 2008 to December 2013) [*Cesana and Chepfer*, 2013]. Red (blue) shading represents ice-dominated (liquid-dominated) grid cells. A hundred percent means ice clouds only, whereas 0% means liquid clouds only. The last three panels are, respectively, the multimodel standard deviation, the multimodel mean, and the observations. The solid (dashed) yellow and green lines correspond to the 90% phase ratio isocontour (PR90) (±1 standard deviation) as observed by CALIPSO-GOCCP and as simulated by each GCM, respectively. The white dashed lines separate the low-level and mid-level clouds (3.2 km), and mid-level and high-level clouds (6.5 km).

meaning that there is only liquid in the grid cell, whereas the pink shading represents a PR of 100%, meaning that there is only ice in the grid cell. Figure 3 also shows the PR90 line (green for models and yellow for observations). In the observations, the height of the PR90 line is the highest in the tropics and decreases poleward, following the temperature profile increase. We remind the reader that model-to-model comparison of all features on the plot (e.g., contour shading and green PR90 lines) are appropriate but that comparison between models and observations is most appropriately focused on the green and yellow PR90 lines. Except for MPI-ESM and NCHU (which is based on the previous version of the MPI-ESM atmospheric component), the models simulate similar behavior for PR90. The Beijing Climate Center Atmospheric General Circulaton Model version 2.1 (BCCAGCM2.1), the Community Climate System Model version 4 (CCSM4), and Goddard Earth Observing System version 5 AGCM model (GEOS5-AGCM) overestimate the PR90 height at all latitudes (as well as the mean value, 8.7 km/9.2 km/9.2 km versus 8.6 km), while Iowa State University model (ISU), MPI-ESM, Meteorological Research Institute AGCM model (MRI-AGCM), and NCHU overestimate the height in polar regions. Except BCCAGCM2.1, CCSM4, and GEOS5-AGCM, the PR90 height mean is underestimated, particularly in the tropics. This suggests that the amount of liquid is too low in the middle and high troposphere relative to the total amount of condensed water. The least biased models are CanCM4 (non-*T*-dependent) and the three models derived from the CAM3 core (BCCAGCM2.1, CCSM4, and ISU) that has a *T*-dependent linear relation (between −10°C and −40°C) to split the water content into liquid and ice. On the contrary, the most unrealistic models are IPSL-CM5A and ECearth3 that are also *T*-dependent models, but allow mixed-phase clouds from 0°C to −15°C and −23°C, respectively. Thus, a *T*-dependent linear relation in cloud phase parameterizations can produce realistic cloud phase transition in terms of height if it allows liquid to form up to −40°C. However, there is some ice in clouds at temperatures warmer than 0°C for all models except the strictly *T*-dependent ones (BCCAGCM2.1, CCSM4, CNRM, IPSL-CM5A, and ISU). This could be due to the presence of solid precipitation, which for most models is set to melt for temperature warmer than 2°C compared to 0°C in

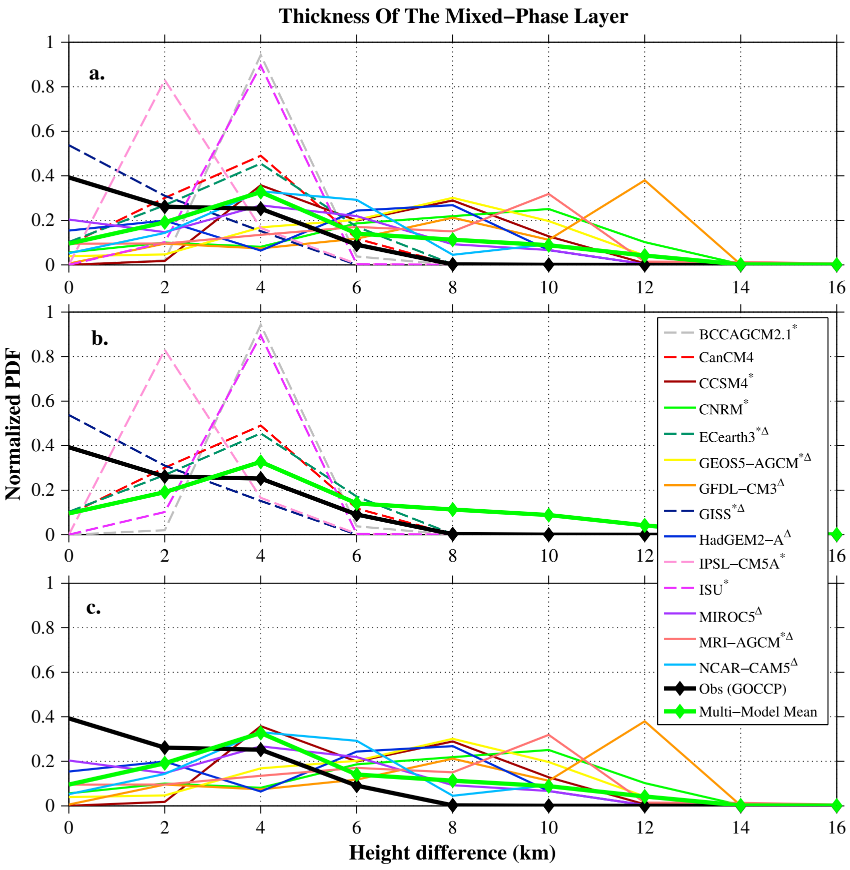

Figure 4. (a) Normalized probability density function (*y* axis, PDF) of mixed-phase layer thickness (*x* axis, km) simulated by 16 GCMs (colored lines) and observed by CALIPSO-GOCCP (black diamond line) between 20°S and 20°N. (b) The models (dashed lines) that simulate a single peak below 6 km. (c) The models (solid lines) simulating one or multiple peaks, with the largest thickness of mixed-phase cloudy layer. This figure has been computed using 1 year of simulation (daily data) and 6 years of observations (daily data; 2008–2013). The mixed-phase layer is defined as the layer containing both liquid and ice cloud particles ($0\% < PR < 100\%$; typically the blue to red shading in Figure 3). The green diamond line is the multimodel mean. See the legend for the GCM's name.

strictly *T*-dependent models. Note that for MPI-ESM and NCHU, it happens very close to the surface. The interpolation onto the GASS-YoTC/MJOTF grid enhanced this phenomenon already present in the original model outputs.

The geometrical thickness of the mixed-phase layer is a key parameter to accurately compute radiation scattering and absorption by clouds and thus, the surface and top of the atmosphere fluxes as well as heating rate profiles. Although caution needs to be exercised in comparing CALIPSO-GOCCP to the simulations, we can argue that the thickness of the CALIPSO-GOCCP mixed-phase area will give an estimate of the minimum thickness expected. This low bias to the observed thickness occurs because the lidar does not penetrate through clouds with an optical thickness higher than three [*Chepfer et al.*, 2013], and thus, CALIPSO-GOCCP cannot document the lowest clouds when dense clouds (liquid or ice) overlap them. The undetected lowest clouds can potentially have a different phase of the above-detected clouds and thus increase the thickness of the mixed-phase area. CALIPSO-GOCCP mixed-phase thickness hence represents a minimum that could be slightly larger if the CALIPSO lidar was able to detect all clouds. In this regard, a model's mixed-phase thickness should be at least as large as that indicated by CALIPSO-GOCCP.

Since Figure 3 is a zonal mean, it is not representative of different regimes (e.g., ascending and descending branches of the Walker circulation). To avoid any averaging effect, we computed the probability distribution functions (PDFs) of the instantaneous vertical thickness of the mixed-phase layer in Figure 4, using 365 daily values at every grid point between 20°S and 20°N. The mixed-phase vertical thickness is defined as the difference between the height of the grid cell with the lowest PR value (still higher than 0%, closest to the surface) and the grid cell with the highest value (still lower than 100%) in the same profile. That definition includes discontinuous clouds, as GCMs do not simulate clouds but rather cloudy grid boxes. This provides us information on the layer thickness in which mixed-phase clouds can form, which is much thinner than the total cloud thickness [e.g., *Cesana and Chepfer*, 2013, Figure 7c]. Because of the lidar limitation (discussed above), the maximum thickness of the observed distribution (Figure 4: 6 km) could be underestimated in observations and, consequently, the most frequent values, ranging between 0 (meaning only one 480 m layer of mixed-phase cloud) and 4 km, could be overestimated. Yet the maximum should not be much larger than 6 km, since the base of the mixed-phase cloudy layer always corresponds to the freezing temperature (0°C; not shown), and hence, no ice could form below this level. The models show two distinct distributions with peaks below and above 6 km. The models with the smallest mixed-phase cloudy layers (Figure 4b) show a single peak (BCCAGCM2.1, CanCM4, ECearth3, Goddard Institute for Space Studies (GISS), IPSL-CM5A, and ISU), as opposed to the other models (Figure 4c; CCSM4, CNRM, GEOS5-AGCM, Geophysical Fluid Dynamics Laboratory–Coupled Model version 3 (GFDL-CM3), the atmospheric component of the Hadley Global Environment Model version 2 (HadGEM2-A), the Model for Interdisciplinary Research on Climate version 5, MRI-AGCM, and NCAR-CAM5), which show multiple peaks. These multiple peaks are linked to precipitation generated in the deep convection regimes, corresponding to ascending branches of the Walker circulation (South America, South Africa, and the Western Pacific). As mentioned earlier, MPI-ESM and NCHU models simulate a slight amount of ice in clouds at low levels even at the surface in the tropics, resulting in a mixed-phase layer often very large (typically larger than 10 km). Since this behavior is not realistic, we do not take into account these two models in the multimodel mean. Only two models (GISS and IPSL) underestimate the thickness of the mixed-phase layer in the tropics compared to the observations. Finally, keeping in mind the caveats when using the observations—i.e., an underestimation of the largest mixed-phase layers and a maximum not much larger than 6 km—CanCM4 and ECearth3 are the models the closest of the observed thickness of mixed-phase cloudy layer. Furthermore, 10 models over estimate the thickness of the mixed-phase cloudy layer (CCSM4, CNRM, GEOS5-AGCM, GFDL-CM3, HadGEM2-A, MIROC5, MRI-AGCM, and NCAR-CAM5).

3.2. Temperature

The observed phase transition between the three thermodynamic states of water is strongly related to the temperature but also dependent on pressure, particle size, type of nucleation, etc. In theory, the temperature for homogenous nucleation of supercooled liquid droplets occurs around −40°C and may vary slightly as a function of the particle size [*Wallace and Hobbs*, 2006]. Previous studies have identified a substantial amount of liquid in clouds at temperature ranging between −40°C and −30°C, using airborne in situ measurements at midlatitudes [e.g., *Korolev et al*., 2003] or using ground-based observations in the Arctic [e.g., *Shupe*, 2011]. However, it is not clear what the expected amount of liquid in clouds should be with respect to the total condensate near this temperature and at scales commensurate with GCM representations. To examine this relation and facilitate the analysis of the cloud phase schemes under study, we computed the PR for 3°C temperature bins instead of the height at every grid point.

Figure 5 depicts the result as a zonal mean. CALIPSO-GOCCP observations indicate that the zonal mean of the PR90 line (yellow solid line) is relatively constant with temperature, occurring between −30°C and −35°C. At these temperatures, there is slightly more liquid in the midlatitudes and polar region than in the tropics, or put another way the PR90 occurs at slightly lower temperatures at high latitudes than the tropics. At warmer temperatures (~−5°C), the Antarctica plateau shows relatively high amounts of ice cloud. However, this is not surprising given the thermodynamic conditions of this region (cold and dry), which differ greatly from the rest of the Earth. The global mean PR90 is −33.7°C (±1.4). The multimodel mean of the PR90 line (green solid line) is close to the observed one (−32.2°C, ±1.5). However, the gap between the yellow and green lines can vary significantly as a function of latitude for the models that do not employ a *T*-dependent scheme, whereas it is fairly stable for *T*-dependent models (marked with a star, except MRI-AGCM). Models that simulate an increasing liquid proportion toward the poles (CanCM4, GEOS5, GFDL-CM3, GISS, MIROC5, MPI-ESM, MRI-AGCM, and NCHU) agree better with observations. These models include either the BF mechanism (marked with a delta) or complex microphysics in their cloud phase parameterization. The best are CanCM4 and GEOS5-AGCM. They can mimic the zonal dependence within a range of ±6°C of the observed mean. There are a number of models (i.e., CanCM4, ECearth3, HadGEM2-A, MIROC5, and NCAR-CAM5) exhibiting little or no supercooled liquid at temperatures just below freezing, over Antarctica, where sea ice and ice sheets are

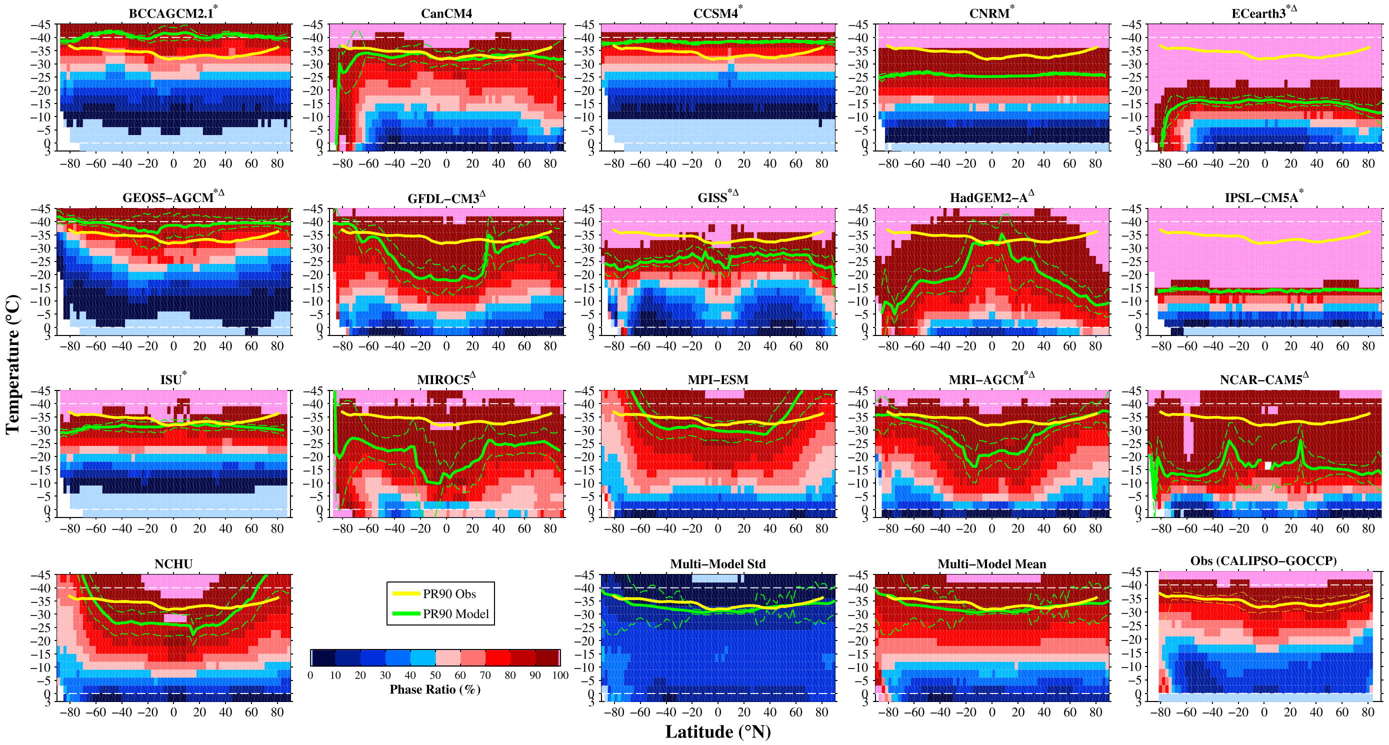

Figure 5. Annual and zonal mean (*x* axis, °N) temperature profiles (*y* axis, °C) of cloud phase ratio (PR, %) simulated by 16 GCMs (Mass Phase Ratio, MPR) and observed by CALIPSO-GOCCP (Presence Phase Ratio, PPR; January 2008 to December 2013) [*Cesana and Chepfer*, 2013]. Red (blue) shading represents ice-dominated (liquid-dominated) grid cells. A hundred percent means ice clouds only, whereas 0% means liquid clouds only. The last three panels are, respectively, the multimodel standard deviation, the multimodel mean, and the observations. The solid (dashed) yellow and green lines correspond to the 90% phase ratio isocontour (PR90) (±1 standard deviation) as observed by CALIPSO-GOCCP and as simulated by each GCM, respectively. The white dashed lines are the −40°C and 0°C isotherms.

present all year, in agreement with observations. HadGEM2-A, MIROC5, and NCAR-CAM5 are the models with the smallest liquid proportion between 0°C and −40°C. The ice phase dominates almost everywhere at temperature below −6°C. Yet this does not prevent liquid droplets to form at very low temperature (for instance, HadGEM2-A shows little liquid amount around −30°C) compared to *T*-dependent models such as ECearth3 and IPSL-CM5A. The lack of supercooled liquid at very low temperature (typically below −25°C) may lead to radiation biases over the Southern Ocean in some models [*Forbes and Ahlgrimm*, 2014]. Putting aside the observations, and PR90, for a moment to compare the full temperature and latitude dependence of the modeled PR, the level of disagreement in this characteristic—i.e., a simple indicator of cloud phase—is quite astounding. Comparison of any set of models across a given column or row exhibit remarkable differences.

Figure 6 shows the annual mean of the PR90 lines along with the observations for different regions: the polar regions (poleward 60°S/N, blue bars), the midlatitudes (between 60°S/N and 30°S/N, red bars), and the tropics (between 30°S and 30°N, green bars). Most models (all but CCSM4, CNRM, and IPSL-CM5A) exhibit distinct annual mean temperatures for PR90 depending on the region, in agreement with the observations. However, only few of them are able to capture the observed tendency, i.e., the increase of the PR90 temperature from the poles to the equator. Those are GEOS5-AGCM, GFDL-CM3, MPI-ESM, MRI-AGCM, and NCHU. Three models (BCCAGCM2.1, CCSM4, and GEOS5-AGCM) clearly underestimate annual mean temperatures for PR90 compared to observations (in average, −40.8°C, −38.3°C, and −37.9°C versus 33.7°C) as opposed to the 13 other models that overestimate it. This means that the majority of the models do not produce enough liquid at very low temperatures (up to −40°C).

3.3. Relative Humidity and Vertical Wind

In that section, we further investigate the dependence of the cloud phase transition on other environmental variables such as the relative humidity and the vertical velocity. Those two variables strongly affect GCM

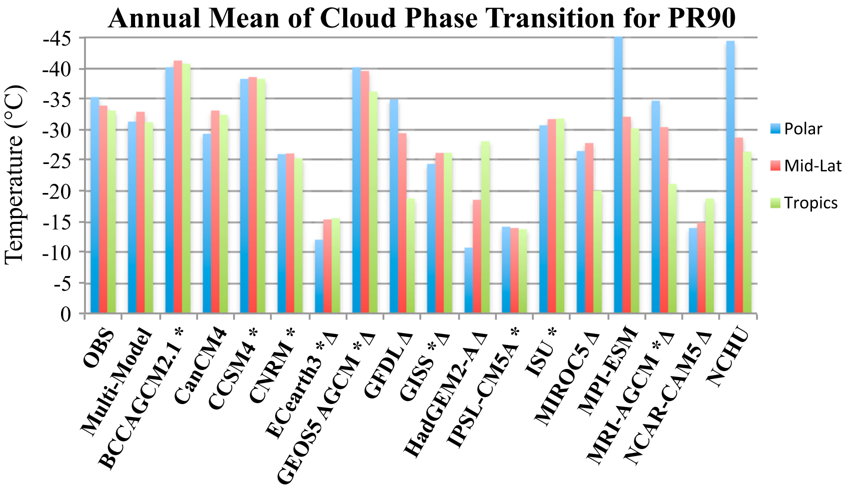

Figure 6. Annual mean temperature (*y* axis, °C) of the cloud phase ratio at 90% (PR90) simulated by 16 GCMs (*x* axis) and observed by CALIPSO-GOCCP (January 2008 to December 2013) [*Cesana and Chepfer*, 2013] for three regions: the polar regions (poleward 60°S/N; blue bars), the midlatitudes (between 60°S/N and 30°S/N; red bars), and the tropics (between 30°S and 30°N; green bars).

cloud formation and properties and could therefore influence the cloud phase transition. We show the annual mean temperature profiles of the PR as a function of relative humidity in Figure 7. We averaged and interpolated the European Centre for Medium-Range Weather Forecasts Reanalysis (ERA-Interim) [*Dee et al.*, 2011] relative humidity fields (dz = 25 hPa, dx = 0.75°, 6-hourly) onto the same spatial-temporal

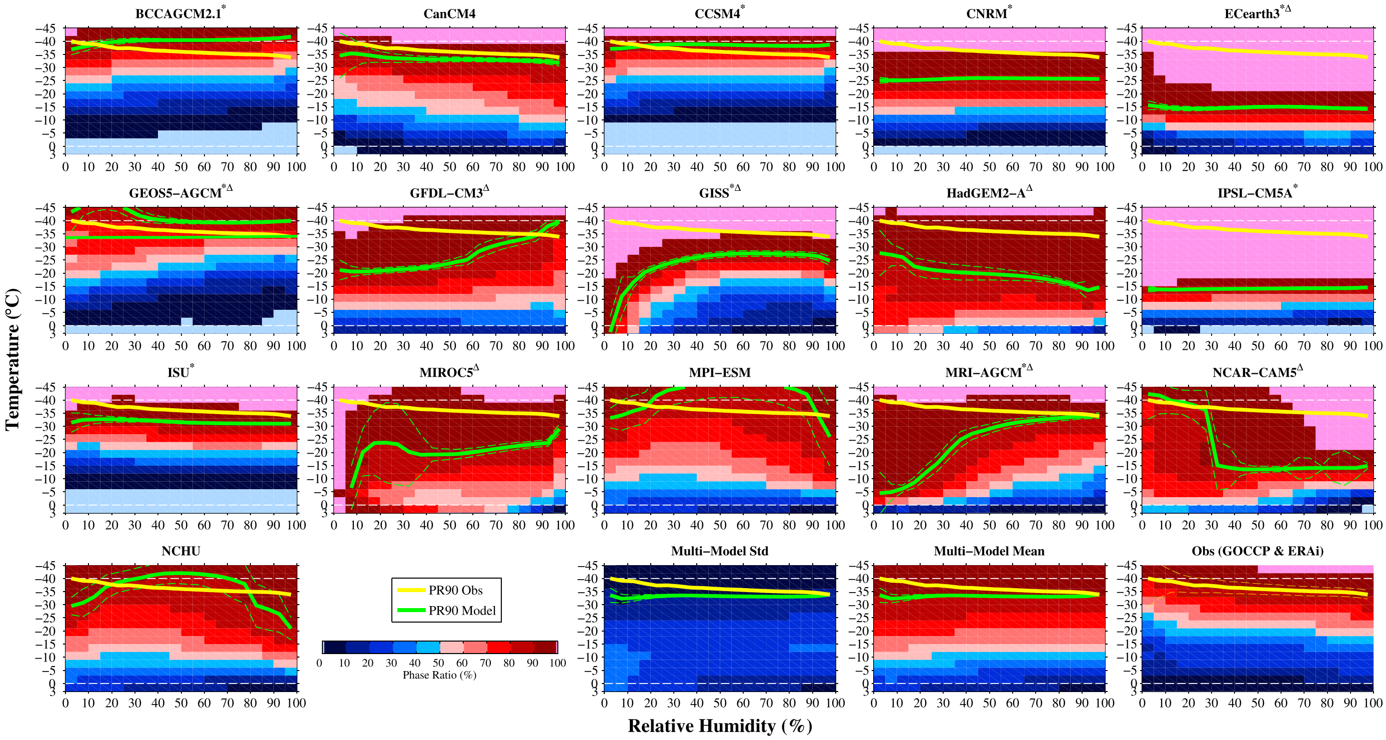

Figure 7. Annual mean temperature profiles (*y* axis, °C) of cloud phase ratio (PR, %) against relative humidity (*x* axis, %) simulated by 16 GCMs (Mass Phase Ratio, MPR) and from ERA-Interim Reanalysis (January 2008 to December 2013) [*Dee et al.*, 2011] and CALIPSO-GOCCP observations (Presence Phase Ratio, PPR; January 2008 to December 2013) [*Cesana and Chepfer*, 2013]. Every bin is statistically representative as it contains more than several hundred points. The last three panels are, respectively, the multimodel standard deviation, the multimodel mean, and the observations. The solid (dashed) yellow and green lines correspond to the 90% phase ratio isocontour (PR90) (±1 standard deviation) as observed by CALIPSO-GOCCP and as simulated by each GCM, respectively. The white dashed lines are the −40°C and 0°C isotherms.

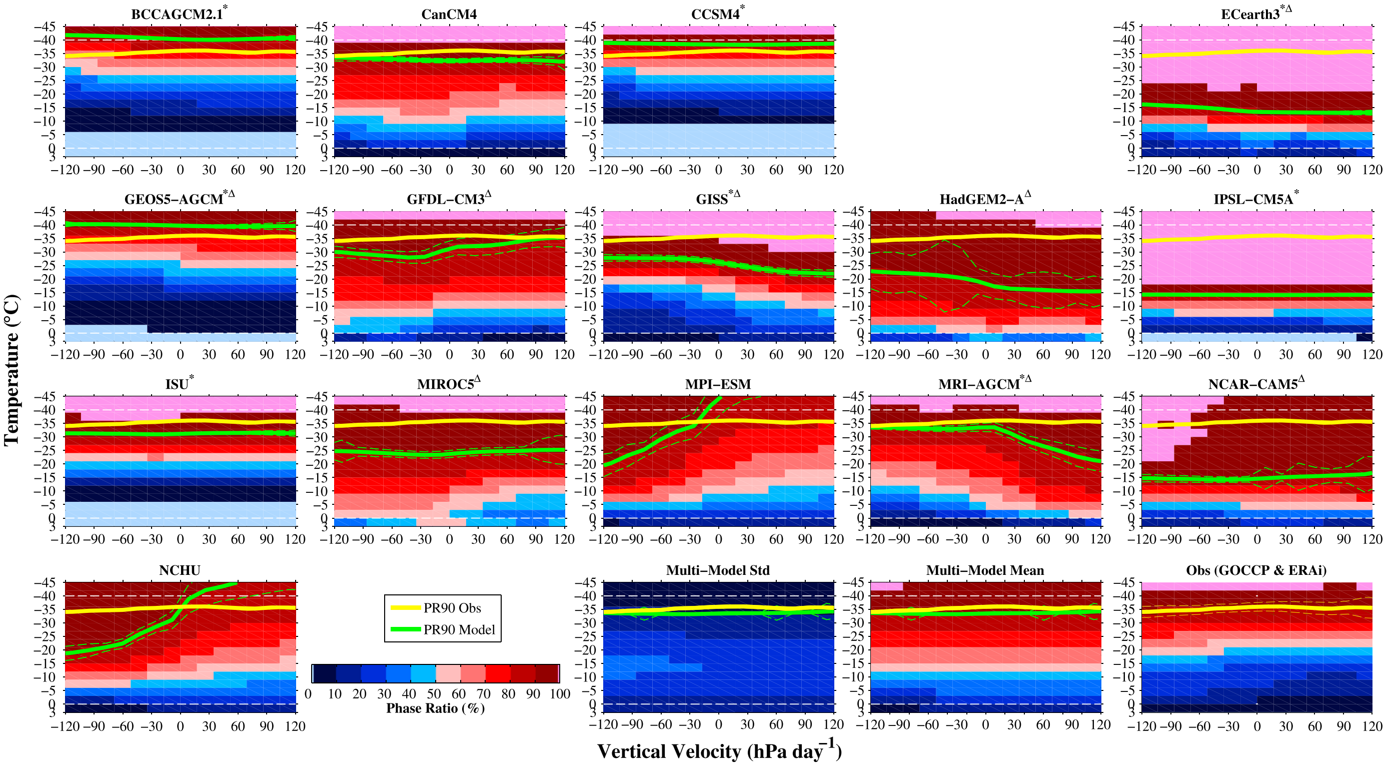

Figure 8. Same as Figure 7 for vertical wind speed (*x* axis, hPa day^{-1}) instead of relative humidity.

grid as CALIPSO-GOCCP ($dz = 480$ m, $dx = 2.5°$, daily), and combined it with CALIPSO-GOCCP to get the observation panel (Figure 7, bottom right). The observed PR90 slowly decreases as the relative humidity increases (no matter the region under study, i.e., tropics, midlatitude, or poles). The multimodel mean depicts the opposite behavior while only CanCM4 and HadGEM clearly reproduce the observed relation, whereas NCAR-CAM5 barely simulates a decrease and MPI-ESM and NCHU simulate an increase from 0% to 50% and then a decrease. The rest of the models simulate either the opposite relation or no variations at all. As with the dependence on temperature alone, these intermodel differences are huge and point to fundamental uncertainties and flaws in cloud (phase) modeled (or parameterized) physics.

As many studies have shown a critical dependence of the cloud regime on large-scale vertical velocity [e.g., *Bony et al*., 2004; *Wyant et al*., 2006], we have calculated the dependence of the large-scale vertical velocity as a function of temperature and latitude. Indeed, the subgrid vertical velocity (typically calculated via parameterization based on the large-scale vertical velocity and other quantities) modulates the degree of supersaturation and therefore the activation of aerosol particles. Previous studies pointed out the influence of the in-cloud vertical velocity on the water content [e.g., *Tonttila et al*., 2013]. For example, *West et al*. [2014] concluded that increasing the subgrid vertical velocity leads to an increase of the liquid water path. Figure 8 shows the annual mean temperature profiles of the PR as a function of large-scale vertical velocity for the 16 models and for ERA-Interim reanalysis combined with CALIPSO-GOCCP PR. In the observations (Figure 8, bottom right), the updrafts (negative vertical velocity) correspond to slightly warmer cloud phase transition (PR90) than the downdrafts (positive vertical velocity), meaning that rising air supports the ice crystals formation over liquid droplets for decreasing temperatures. The same trend is observed at different latitudes (tropics, midlatitudes, and poles). The multimodel mean PR90 exhibits no particular variation in either the subsiding or ascending regimes. However, similar to relative humidity versus PR90, the link between vertical velocity and PR90 is not well reproduced by the models. Only five models (GFDL-CM3, MIROC5, MPI-ESM, NCAR-CAM5, and NCHU) are in agreement with observed tendency of the PR90 line. We found similar results using Arctic region data—i.e., less convective motions—meaning that the "PR-relative humidity" and "PR-vertical velocity" relations are not governed by the convective schemes.

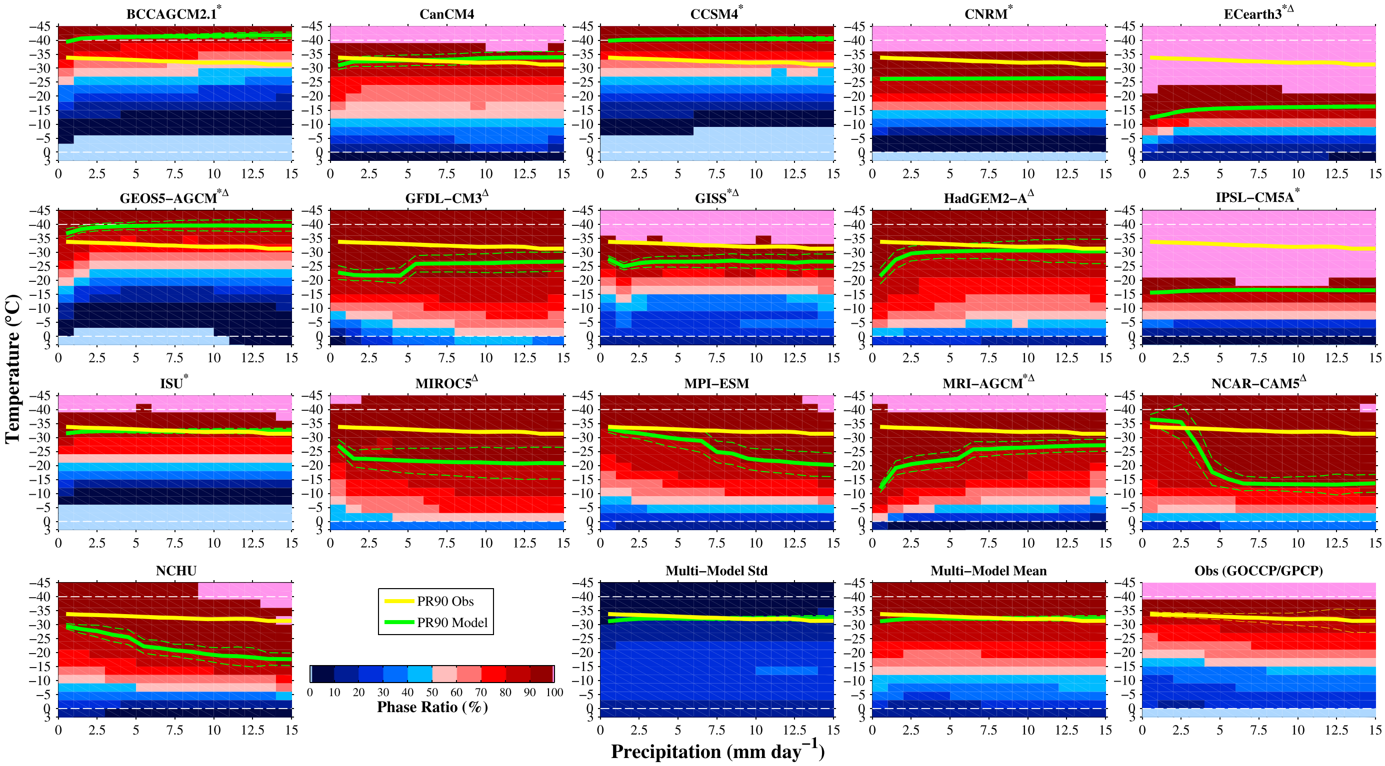

Figure 9. Annual mean temperature profiles (*y* axis, °C) of cloud phase ratio (PR, %) against precipitation (*x* axis, mm d^{-1}) simulated by 16 GCMs (Mass Phase Ratio, MPR) and using GPCP (January 1996 to December 2008) [*Huffman et al.*, 2001] and CALIPSO-GOCCP observations (Presence Phase Ratio, PPR; January 2008 to December 2013) [*Cesana and Chepfer*, 2013]. Every bin is statistically representative as it contains more than several hundred points. The last three panels are, respectively, the multimodel standard deviation, the multimodel mean, and the observations. The solid (dashed) yellow and green lines correspond to the 90% phase ratio isocontour (PR90) (±1 standard deviation) as observed by CALIPSO-GOCCP and as simulated by each GCM, respectively. The white dashed lines are the −40°C and 0°C isotherms.

The overall vertical velocity versus PR diagram is quite different depending on the models as well. The vertical velocity can have a strong impact on the PR for GISS, MIROC5, MPI-ESM, MRI-AGCM, and NCHU models. The complex aerosol schemes of these later models, which account for the direct and indirect effects of aerosols on microphysics, could help explain the sensitivity of the model to the vertical velocity. Aerosol activation is based on the number, the particle size and the chemical properties of aerosols as well as the vertical updrafts [e.g., *Donner et al.*, 2011; *Lohmann and Roeckner*, 1996; *Takemura et al.*, 2005].

3.4. Precipitation

The precipitation and related processes (autoconversion, freezing/melting, and collection) may introduce changes in the liquid/ice water content and modify the cloud phase transition, even for *T*-dependent models. Figure 9 shows the annual modeled PR for different precipitation rates, at the surface, as a function of the temperature and between 40°S and 40°N. The observed relation between cloud phase and precipitations (Figure 9, bottom right) has been constructed from Global Precipitation Climatology Project (GPCP version 1DD) [*Huffman et al.*, 2001] daily values (1° × 1° grid interpolated onto the 2.5° × 2.5° CALIPSO-GOCCP grid) along with CALIPSO-GOCCP data. The observations show relatively small impact of the precipitation on the cloud phase transition. On average, the transition from liquid to ice appears at warmer temperatures when precipitation occurs. Similar results have been found using Tropical Rainfall Measurements Mission data [*Huffman et al.*, 2007] (more sensitive to light precipitation) for precipitation (not shown).

In all the participating models, precipitation is diagnosed, which means its time derivative is neglected. However, precipitation is simulated based on the same set of processes with different degrees of complexity. First, the precipitation is triggered by autoconversion. Once present, the rain and/or snow collect other cloud particles and grow. Then, the change of phase of the precipitating hydrometeors is considered: snow can melt/sublimate, rain can freeze/evaporate. On top of that, some models also consider the influence of one phase on the other, for instance, through the BF process. The parameterizations chosen to represent those processes are considerably different. As a consequence, the feedbacks induced by the presence of precipitation on the cloud phase transition may be the opposite from one model to another.

In the present study, the multimodel mean of the cloud phase transition for PR90 exhibits no particular variation but the models can be sorted in three groups. In the first group, precipitation has virtually no relation with the cloud phase transition (CanCM4, CCSM4, CNRM, GISS, ISU, and IPSL-CM5A). For these models (except CanCM4), the water phase of precipitation and clouds is partitioned strictly according to the temperature (*T*-dependent models marked with a star). However, this does not prevent the precipitation from being related to other variables on the same time step. For instance, in IPSL-CM5A, CCSM4, and ISU models, the precipitation is evaporated in part and added to the water content of the grid cell below. In the two other groups, the falling hydrometeors can modify cloud phase relationship in the grid cells below. For the second group, MIROC5, MPI-ESM, NCAR-CAM5, and NCHU, the more precipitation is simulated, the less supercooled liquid, and greater proportion of ice, at low temperatures. For the third group: BCCAGCM2.1, ECearth3, GEOS5-AGCM, GFDL-CM3, HadGEM2-A, and MRI-AGCM, the opposite behavior to this occurs. For these models, the more precipitation, the proportion of liquid (ice) increases (decreases) as temperature increases. Finally, the observations for PR90 suggest that the second group of models (i.e., MIROC5, MPI-ESM, NCAR-CAM5, and NCHU) has a more realistic representation of the PR90 relationship relative to precipitation.

The dependence on the precipitation does not show the same diversity of response for the PR-precipitation diagram as compared to relative humidity and vertical velocity. The fact that the precipitation is diagnosed rather than prognosed seems to limit the impact on the cloud water content as well as the cloud phase transition.

For some models, it is easy to identify processes that lead to the variation in PR versus precipitation discussed above. For instance, in NCAR-CAM5, all the rain freezes instantaneously when the temperature drops below −5°C, which means, as the rain increases the IWC increases. In GFDL-CM3, vapor first condensates into liquid phase and then is partitioned through a strong, but not solely, *T*-dependent relation. The presence of solid precipitation triggers further ice cloud formation as well. That is why the IWC increases at all temperature with increasing precipitation. GEOS5 utilizes an autoconversion rate that depends on the cloud type and the phase of the precipitating particle. Therefore, light precipitation associated with low stratiform clouds (liquid) generates a different cloud phase transition profile than heavy precipitation coming from deep convective clouds.

3.5. An Illustrative Method to Compare Cloud Phase Schemes

In the literature, several studies have examined the PR as a function of the temperature to better understand what governs the cloud phase transition [e.g., *Bower et al*., 1996; *Korolev et al*., 2003; *Hu et al*., 2010]. This representation is a useful way to compare the multiple cloud phase schemes of the models. Here we propose an augmentation to this temperature-only perspective by adding the cloud phase frequency of occurrence. Fortunately, the CALIPSO-GOCCP observations provide some measure of reality that can be used to assess model fidelity, particularly for very high PR values (as discussed earlier). Figure 10 shows the global frequency of occurrence (relative to all cloudy pixels between −45°C and 3°C) of clouds as a function of the PR (vertical axis) and the temperature (horizontal axis) of the grid point, all over the globe. The PR bins range from 0 to 100% every 10%, and the temperature bins are 3°C with a range of −45°C to 3°C. An advantage of using the frequency of occurrence is that the cloud phase schemes are more readily comparable and the large-scale processes as well as the convective (small-scale) processes are represented on the same figure since we accumulate occurrences instead of averaging, as done in most studies.

The mean observed phase-temperature relation (Figure 10 (bottom right), magenta line, and replicated on all other panels) is almost linear from 0°C to −40°C. Significant liquid-only cloud occurrences (i.e., PR = 0%) occur up to −34°C, while significant ice-only clouds form up to −12°C and to a lesser extent until the freezing level. This relatively large amount of ice clouds between 0°C and −12°C help to understand the observed bump in the mean phase-temperature relation (magenta line). The majority of liquid-containing clouds occurs at temperatures warmer than −20°C but may form up to −40°C. Besides, the mixed-phase clouds have a frequency of occurrence lower than the liquid-only and ice-only clouds. However, the observed phase-temperature relation may be impacted by the biases of the lidar instrument. *Cesana and Chepfer* [2013, Figure 10b] (see also Figure 1, solid lines versus dashed lines) show the effect of the lidar simulator on the PR of the IPSL model that may sharpen the slope of the mean phase-temperature relation and shift it into colder temperature This is because of (i) the differences between MPR and FPR, as explained in section 2.3, (ii) CALIPSO-GOCCP algorithm is only able to diagnose a cloudy

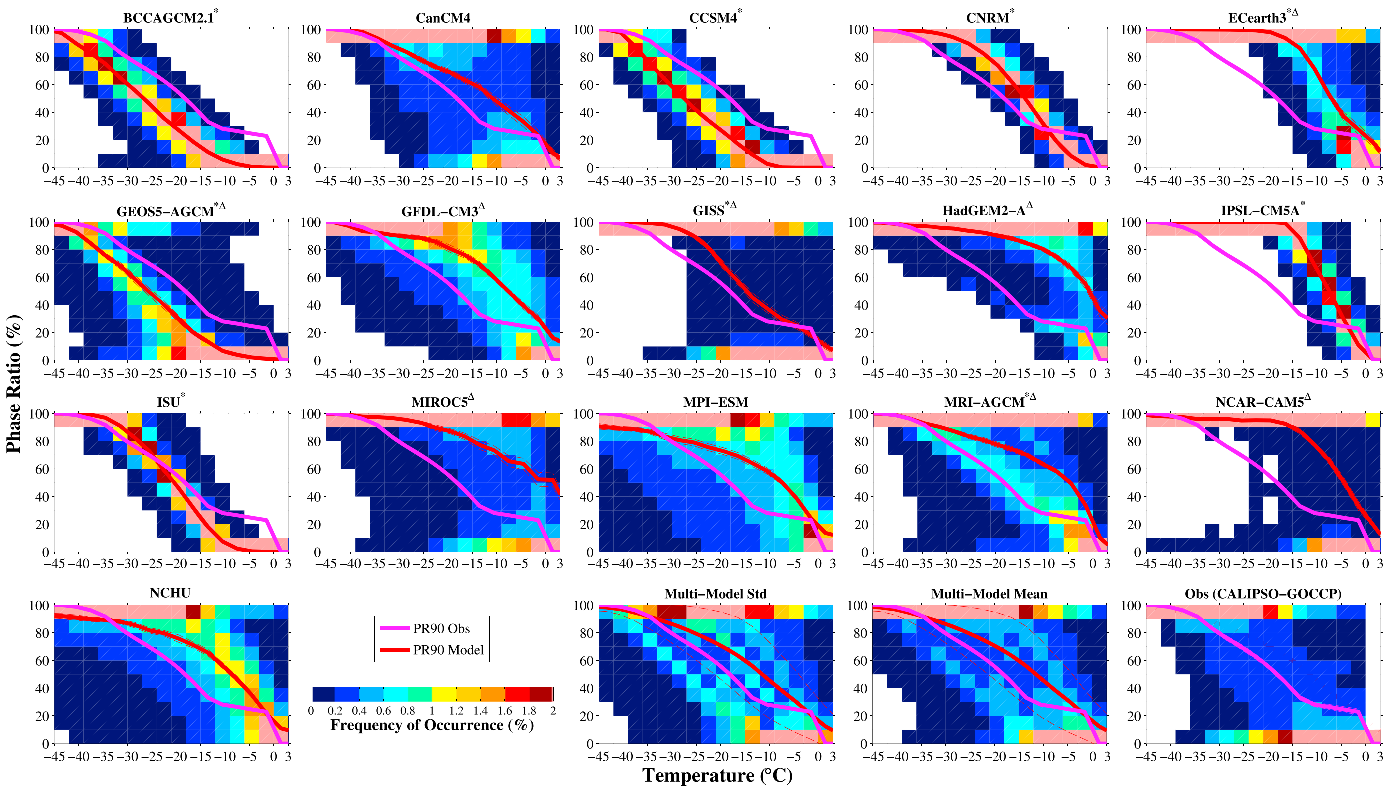

Figure 10. The global frequency of occurrences (%) of cloud phase ratio (PR, %; *y* axis), relative to the total number of cloud events occurring between −45°C and 3°C, against temperature (°C; *x* axis) simulated by 16 GCMs (Mass Phase Ratio, MPR) and observed by CALIPSO-GOCCP (Presence Phase Ratio, PPR) [*Cesana and Chepfer*, 2013]. This figure has been made by accumulating 1 year of daily simulations and 6 years of daily observations (2008–2013) into 3°C temperature bins and 10% PR bins, all over the globe. The last three panels are, respectively, the multimodel standard deviation, the multimodel mean, and the observations. The solid (dashed) magenta and red lines correspond to the relationship (annual mean) between temperature and Phase Ratio (±1 standard deviation) for CALIPSO-GOCCP observations and for each GCM, respectively.

pixel as liquid or ice and not as mixed-phase, and (iii) the phase diagnosed by CALIPSO-GOCCP for mixed-phase clouds is most likely the cloud top phase (G. Cesana et al., submitted manuscript, 2015), which may lead to an overestimation of not only the liquid-only cloudy pixels (PR = 0%) but also ice-only cloudy pixels (PR = 100%; as mentioned in section 2.2).

The *T*-dependent cloud phase models (marked with a star) exhibit a very distinct pattern, which produce more mixed-phase clouds than the observations and non-*T*-dependent models. For a given PR value, the variation of the temperature around the mean phase-temperature relation (solid red line) is low (typically ±5°C) for the *T*-dependent models, compared to other models (up to ±15°C). The mean phase-temperature relations of BCCAGCM2.1, CCSM4, and GEOS5 (also some part of ISU) are colder than the observed one, consistent with the global mean temperature for PR90. Particular patterns stem from non-*T*-dependent models as well. For example, MIROC5 and NCAR-CAM5 simulate almost no mixed-phase clouds. HadGEM2-A, MIROC5, and NCAR-CAM5 simulate very few liquid clouds at temperatures lower than −25°C. According to the observations, which are already biased with too many ice-only clouds in warm temperatures (−15°C to 0°C), numerous models (CanCM4, ECearth3, GISS, HadGEM2-A, IPSL-CM5A, MIROC5, MPI-ESM, MRI-AGCM, NCAR-CAM5, and NCHU) have too many ice-only clouds at temperatures warmer than −15°C. As discussed above, the lidar effect sharpens the mean phase-temperature relation by adding a cold bias and overestimates liquid-only and ice-only clouds. Therefore, the "true" phase-temperature relation should be shifted to warmer temperature (difficult to quantify with accuracy, more than 3°C judging from Figure 1), even more for the low PR values, and the overall diagram should include less liquid-only/ice-only cloud occurrences. Therefore, the most likely phase-temperature relation would be close to the multimodel mean, CanCM4, GFDL-CM3, MPI-ESM, and NHCU, and to a lesser extent MRI-AGCM. Those are the models that have a warmer phase-temperature relation compared to observations as well as less ice-only and liquid-only cloud occurrences and are able to simulate liquid at temperatures below −30°C.

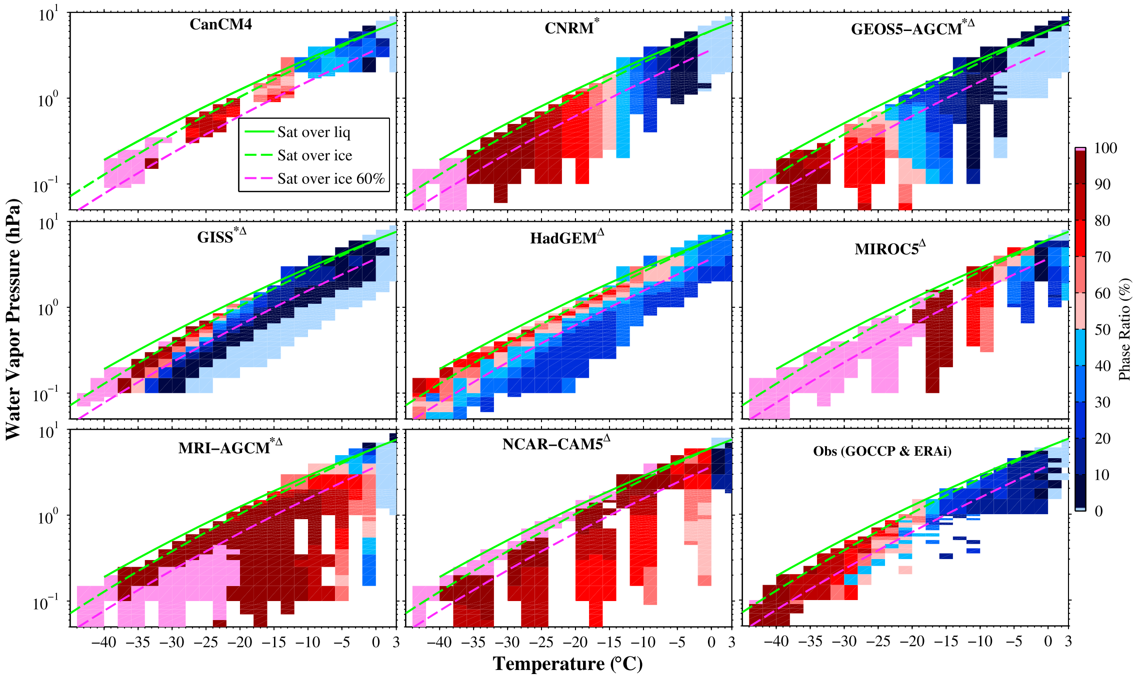

Figure 11. Two-dimensional histograms "Phase diagram" of the cloud phase ratio (PR, %) as a function of the water vapor pressure (semilog *y* axis, hPa) and the temperature (*x* axis, °C) simulated by eight GCMs (Mass Phase Ratio, MPR) and from ERA-Interim reanalysis (November December January 2009–2010) [*Dee et al.*, 2011] and CALIPSO-GOCCP observations (Presence Phase Ratio, PPR; November December January 2009–2010) [*Cesana and Chepfer*, 2013], over the domain 10°S–10°N and 60°E–160°E. The statistically nonrepresentive bins (i.e., frequency of occurrence $< 0.015\%$) have been filtered. The green solid and dashed lines represent the vapor saturation over liquid and vapor saturation over ice relations, respectively, computed from the Clausius-Clapeyron equations (values from *Sonntag* [1990]). The magenta dashed line is the water vapor saturation over ice if the saturation occurred at 60% of relative humidity.

4. Characterization of the BF Process

The Clausius-Clapeyron (C-C) equation describes the three water phases (solid, liquid, and gas) under conditions of thermodynamic equilibrium, in a closed system. The transition curves between the different water phases may be represented by the integrated form of the C-C equation [*Pruppacher and Klett*, 1997, equation (4.79), section 4.8]. The C-C phase diagram represents a good approximation to predict when the water vapor is going to condense to form a cloud. Furthermore, at subfreezing temperatures, it allows predicting at what temperature and water vapor pressure the BF process will occur in mixed-phase clouds, provided that the water vapor and water content are sufficiently high. As a consequence, the C-C phase diagram constitutes a way to characterize the BF process in observations and models, albeit it does not provide any information on the speed and efficiency of the process, which depends on multiple parameters (number of cloud condensation nucleus and ice nuclei (IN), the number and size of the liquid droplets and ice crystals, the speed of the water vapor deposition, the rate of condensational growth, etc.). Contrary to the previous section, here we utilize instantaneous vertical profiles of CALIPSO-GOCCP observations and model simulations (see section 2.1) at every time step and at native model resolution (vertical and horizontal) rather than global mean data. By doing so, we avoid averaging and interpolating (in time and space) and keep as accurate as possible the pattern of the C-C phase diagram.

In observations, we use instantaneous CALIPSO-GOCCP vertical profiles of cloud phase (1:30 P.M. or 1:30 A.M. local time, $dz = 480$ m, $dx = 330$ m, 70 m diameter footprint) and high-resolution ERA-Interim temperature and humidity fields (6-hourly, $dz = 25$ hPa, $dx = 0.75°$), interpolated onto the same CALIPSO-GOCCP spatial-temporal resolution, to build the C-C phase diagram for the observed PR (Figure 11, bottom right). Details of the computation are given in Appendix B. The green and green dashed lines correspond to the saturation vapor pressure over water and over ice, respectively. Therefore, evidence of the BF process at work is illustrated by conditions between these two lines —i.e., a prevalence of the ice over the liquid compared to below the green dashed line. At temperatures warmer than −16°C or colder than −30°C, evidence of the BF process is not obvious. Between −20°C and −28°C, where the ice clouds are more numerous than liquid clouds ($PR > 50$), we can clearly see an increase of the PR values above the ice saturation line (green dashed line) as opposed to the ones toward the 60% saturation line (magenta dashed line). This is the consequence of ice crystals' growth at the expense of the liquid droplets through the BF process. These findings provide support that the BF process plays an important role in the cloud phase partitioning of mixed-phase clouds and can be observed with global satellite data.

We reproduce the C-C phase diagram using high temporal (typically around 15 min) and spatial resolution (native resolution) outputs of eight models (component 2 of the GASS-YoTC/MJOTF experiment (see section 2.1), limited to the domain 10°S–10°N and 60°E–160°E). Except for CNRM-CM5 model, which shows no variations relative to water vapor, the models generally exhibit two distinct behaviors. Although GEOS5-AGCM and MRI-AGCM include the BF mechanism in their microphysics scheme, they tend to predict decreasing PR toward the ice and liquid saturation lines, in contradiction with observations. The lack of samples for CanCM4 model makes it difficult to conclude whether the pattern is statistically representative or not. In contrast, GISS, HadGEM, MIROC5, and NCAR-CAM5 models exhibit the feature characterizing the BF process between the ice and liquid saturation lines, in agreement with observations. This process is particularly well reproduced by GISS model, which simulates a strong BF effect as the PR values exceed 50% below -18°C. On the other hand, it seems to be too strong in HadGEM and NCAR-CAM5 models; i.e., the PR change toward the ice saturation line is too sharp at a constant temperature. Reducing the ice deposition rate (i.e., the efficiency of the BF process) could enhance the supercooled liquid cloud frequency in closer agreement with observations [e.g., *Forbes and Ahlgrimm*, 2014].

5. Summary

In this paper, we take advantage of the active lidar sensing capability of the CALIPSO satellite data (i.e., CALIPSO-GOCCP product), as well as passive satellite data (GPCP) and reanalysis data (ERA-Interim) to compare and evaluate the cloud phase transition representations in 16 GCM simulations that were contributed to one of two multimodel experiments (GASS-YoTC/MJOTF or CMIP5-AMIP). The analysis is based on the cloud phase ratio (PR). The PR is defined as the ratio of the IWC to the sum of the LWC and the IWC for climate models (i.e., Mass Phase Ratio, MPR) and as the ratio of the ICF to the sum of the ICF and the LCF for observations (i.e., Frequency Phase Ratio, FPR). We utilized the MPR and FPR values of 90% (referred as PR90) to minimize the differences between the two quantities and to allow a meaningful and consistent comparison (section 2.3) in the absence of simulator. We then analyzed the performance of the models in reproducing the observed relation of the cloud phase transition for PR90 and some environmental variables (relative humidity, vertical velocity, precipitation, and temperature). The main results are gathered in Figure 12 and described below:

1. Although the PR90 multimodel mean of temperature (Figure 4) and height (Figure 3) are within the range of the uncertainty (32.2°C versus 33.7°C and 8 km versus 8.6 km), 13 of the 16 models (red color in the fourth column of Figure 12) underestimate the presence of liquid in mixed-phase clouds at very low temperatures ($T < -25$°C), which correspond to mid-level and high-level clouds ($z > 3.16$ km).
2. Using ERA-Interim reanalysis and CALIPSO-GOCCP, we showed that an increase of the relative humidity is correlated to a decrease of the liquid with respect to all condensate for a given temperature (Figure 7), while most models (11/16) exhibit no variation or the contrary (green and white color in the first column of Figure 12). By conducting similar analysis as a function of the cloud regimes (Figure 8), we illustrated that only 5 of 16 models are able to simulate a warmer cloud phase transition for convective regimes (more humid) than for subsidence regimes (less humid), in agreement with observations (green color in the second column of Figure 12).
3. The study of the relation between precipitation and PR90 using GPCP observations (Figure 9) confirmed the cloud regimes analysis. Warmer cloud phase transition occurs during heavy precipitation (generally associated with convective regimes). Although all models utilize similar processes to simulate precipitation, they do not depict the same features and only four of them agree with observations (red color in the third column of Figure 12).
4. By representing large-scale and convective processes all together in the same plot (Figure 10), we facilitated the comparison of the different cloud phase microphysics schemes. It reveals that the models that do not use a T-dependent cloud phase scheme depict a more realistic pattern (CanCM4, GFDL-CM3, MPI-ESM, and NHCU) than those that do use a T-dependent scheme.

Finally, using non-averaged (in time and space) grid point values from model simulations and instantaneous vertical profiles of satellite observations, we assessed the representation of the BF process in eight models

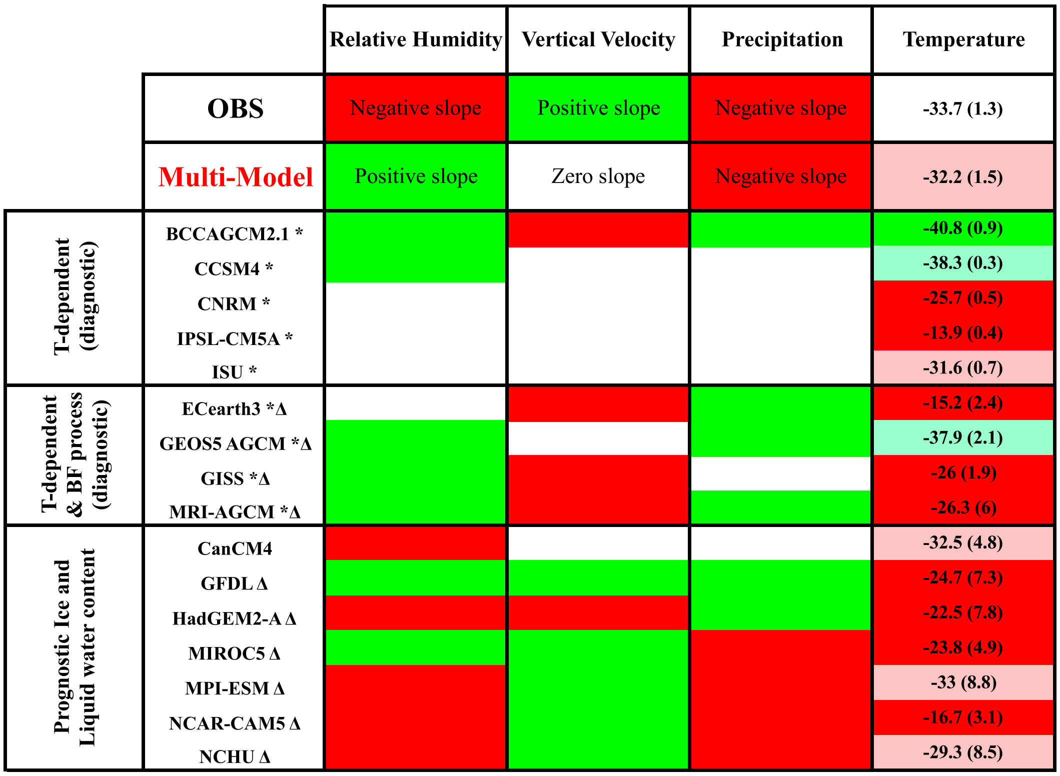

		Relative Humidity	Vertical Velocity	Precipitation	Temperature
	OBS	🟥 Negative slope	🟩 Positive slope	🟥 Negative slope	-33.7 (1.3)
	Multi-Model	🟩 Positive slope	⬜ Zero slope	🟥 Negative slope	-32.2 (1.5)
T-dependent (diagnostic)	BCCAGCM2.1 *	🟩	🟥	🟩	-40.8 (0.9)
	CCSM4 *	🟩	⬜	⬜	-38.3 (0.3)
	CNRM *	⬜	⬜	⬜	-25.7 (0.5)
	IPSL-CM5A *	⬜	⬜	⬜	-13.9 (0.4)
	ISU *	⬜	⬜	⬜	-31.6 (0.7)
T-dependent & BF process (diagnostic)	ECearth3 *Δ	⬜	🟥	🟩	-15.2 (2.4)
	GEOS5 AGCM *Δ	🟩	⬜	🟩	-37.9 (2.1)
	GISS *Δ	🟩	🟥	⬜	-26 (1.9)
	MRI-AGCM *Δ	🟩	🟥	🟩	-26.3 (6)
Prognostic Ice and Liquid water content	CanCM4	🟥	⬜	⬜	-32.5 (4.8)
	GFDL Δ	🟩	🟩	🟩	-24.7 (7.3)
	HadGEM2-A Δ	🟥	🟥	🟩	-22.5 (7.8)
	MIROC5 Δ	🟩	🟩	🟥	-23.8 (4.9)
	MPI-ESM Δ	🟥	🟩	🟥	-33 (8.8)
	NCAR-CAM5 Δ	🟥	🟩	🟥	-16.7 (3.1)
	NCHU Δ	🟥	🟩	🟥	-29.3 (8.5)

Figure 12. Summary of the models' performances in reproducing the observed relation between the cloud phase transition for PR90 and the relative humidity (third column), the vertical velocity (fourth column), precipitation (fifth column), and the temperature (sixth column). The second and third rows are the observations and multimodel mean, respectively. In the three other rows, we separated the models as a function of the degree of complexity of their microphysics scheme. The fourth row gathers the strictly *T*-dependent models, which only use the temperature to distinguish liquid from ice water content in clouds (diagnostically). The fifth row contains T-dependent models as well, but those include the BF process. The last row gathers the models using the more complex microphysics schemes, which prognose the liquid and ice water content in clouds. The colors indicate the slope of the relation between PR90 and the relative humidity, the vertical velocity, and the precipitation: red (green, white) means negative (positive, flat) slope. For the temperature, the red (green) indicates the model overestimates the global mean temperature of the cloud phase transition for PR90. The light red(green) means that the model slightly overestimates (underestimates), within the range of +6°C (−6°C). The scores in the last column (temperature) indicate the global mean temperature of the cloud phase transition for PR90 along with its standard deviation into the brackets. The models that better reproduce the observed relationships along with the most accurate global mean temperatures belong to the third group, i.e., the group using the most complex microphysics schemes.

and the observations through the C-C phase diagram of water vapor (Figure 11). We found evidence that the BF process can be observed at global scale using CALIPSO satellite data. Furthermore, we illustrated that models including this process can replicate the observed C-C phase diagram (GISS and HadGEM) relatively well but not all implementations were realistic (MRI-AGCM and GEOS5-AGCM).

Overall, we showed that intermodel differences in the cloud phase description are very large even though part of this bias could be reduced by using the lidar simulator. Our results underscore the need for observations to constrain the development and evaluation of microphysics parameterizations in GCMs. Noteworthy is that some models can reproduce the relation between cloud phase transition and different variables (height, temperature, humidity, vertical velocity, precipitation, and water vapor pressure). Our results support the fact that the best models are those that include complex microphysics and/or the BF mechanism (Figure 12: the third group of models, bottom row)—i.e., that prognose separately the liquid and ice mixing ratio by taking into account several processes such as condensation/evaporation, deposition, autoconversion, accretion, homogeneous/heterogeneous nucleation, and contact/aggregation. Put another way, a prognostic cloud phase scheme is a necessary condition to reproduce realistic cloud phase transition in GCMs. Some studies have already shown the benefits of doing so [e.g., *Barahona et al.*, 2014; *Forbes and Ahlgrimm*, 2014; *Watanabe*, 2010]. However, some of those models still suffer from a lack of liquid clouds (e.g., HadGEM and NCAR-CAM5).

To understand the causes would necessitate a full sensitivity study based on a restricted number of models. One possibility would be to reduce the deposition rate (i.e., the BF process efficiency [e.g., *Forbes and Ahlgrimm*, 2014]) that seems to deplete too much supercooled liquid in some models (see Figure 11, HadGEM and NCAR-CAM5). Another possibility to improve the liquid fraction would be to reduce the number of ice nuclei (IN), which would also decrease the efficiency of the conversion rate from liquid to ice particles by the BF process [e.g., *Komurcu et al.*, 2014; *Liu et al.*, 2011].

The results obtained in this study provide useful and original tools for the modelers to test and develop their cloud phase scheme at global scale without using the lidar simulator. Utilizing these tools, in addition to other cloud phase products (e.g., CloudSat IWC [*Li et al.*, 2012; *Chen et al.*, 2011], MODIS cloud ice/liquid water path and fraction [*King et al.*, 2013], and microwave satellite ice/liquid water path and precipitations [*Liu and Curry*, 1996]) and complementary evaluation methods (e.g., use of lidar simulators for a full evaluation at every temperatures and heights and not only at PR90), should lead to an improvement of the representation of clouds and related processes in the next generation of GCMs.

Appendix A: Sensitivity Study on the Multiannual Variation of the Modeled PR90

To justify the use of only 1 year of simulation, we computed the standard deviation (σ) of the zonally averaged height of PR90 at all latitude (i.e., green line in Figure 3), over the 20 years of simulation and for eight models of the GASS-YoTC/MJOTF experiment. We then divided the results by the 20 year mean value to illustrate the magnitude of σ relative to the mean. The maximum value of this ratio is lower than 2% in six models and lower than 5% in the other two models. We also computed the correlation between the zonally averaged height of PR90 averaged over 20 years and the zonally averaged height of PR90 for each year. In all models, the correlation is always higher than 0.975. Similar analysis for observations using 6 years of data showed that the maximum σ to mean ratio is also lower than 2% and the correlation between a given annual mean with the long-term mean is always higher than 0.998.

Appendix B: Detailed Calculation of the Clausius-Clapeyron (C-C) Phase Diagram

We used 119 CALIPSO-GOCCP semiorbit files within October to January period of year 2009 and 2010 (same period as component 2 of the GASS-YoTC/MJOTF experiment, section 2.1) with an overpass time of ±30 min around the ERA-Interim corresponding time step. As the two data sets have different spatial resolutions, we had to modify one to match with the other one. We chose to keep the observed resolution as highly resolved as possible and to oversample/interpolate the reanalysis data rather than average the observations. It makes more sense to interpolate a simulated thermodynamic field than to average an observed cloud on a coarser grid which would add noise by creating partly cloudy pixel issues [e.g., *Pincus et al.*, 2012] and artificial mixed-phase clouds. Thus, we oversampled the ERA-Interim temperature and relative humidity onto the CALIPSO-GOCCP horizontal grid by choosing the closest grid cell of every CALIPSO-GOCCP profiles. We then interpolated linearly the ERA-Interim variables onto the CALIPSO-GOCCP vertical grid. We selected the data between 10°S and 10°N and 60°E and 160°E to meet the simulation requirements (component 2 of the GASS-YoTC/MJOTF experiment, section 2.1). Once the sampled and reformatted ERA-Interim data set was created, we binned separately the liquid and ice clouds on the C-C diagram according to their temperature and water vapor pressure. Finally, from these two separate diagrams (occurrences of liquid and ice), we computed the observed PR diagram (ratio of ice occurrences to the sum of ice and liquid occurrences; Figure 11, bottom right).

Acknowledgments
This research was carried out at the Jet Propulsion Laboratory, California Institute of Technology, under a contract with the National Aeronautics and Space Administration. CALIPSO-GOCCP observations were downloaded from the CFMIP-Observation website (http://climserv.ipsl.polytechnique.fr/cfmip-obs/Calipso_goccp.html). ERA-Interim reanalyses were downloaded from ClimServ website (http://climserv.ipsl.polytechnique.fr/fr/les-donnees/era-interim.html). GPCP precipitation data were downloaded from ftp://ftp.cgd.ucar.edu/archive/PRECIP/. The authors thank the climate modeling groups for producing and making available their model outputs from the GASS-YoTC/MJOTF and the CMIP5/AMIP experiments. Special thanks are due to Romain Roehrig (Météo-France, CNRM-GAME) who provided CNRM-CM5 outputs using the simulator for Figure 1. The authors also thank the three anonymous reviewers and the Editor for their relevant comments, which have improved the manuscript.

References

Barahona, D., A. Molod, J. Bacmeister, A. Nenes, A. Gettelman, H. Morrison, V. Phillips, and A. Eichmann (2014), Development of two-moment cloud microphysics for liquid and ice within the NASA Goddard Earth observing system model (GEOS-5), *Geosci. Model Dev. Discuss.*, *6*, 5289–5373, doi:10.5194/gmdd-6-5289-2013.

Bergeron, T. (1935), On the physics of cloud and precipitation, in *Proceeding 5th Assembly U.G.G.I. Lisbon*, vol. 2, 156 pp., Int. Union of Geod. and Geophys., Karlsruhe, Germany.

Bony, S., et al. (2004), On dynamic and thermodynamic components of cloud changes, *Clim. Dyn.*, *22*, 71–86.

Bony, S., M. Webb, C. Bretherton, S. Klein, P. Siebesma, G. Tselioudis, and M. Zhang (2011), CFMIP: Towards a better evaluation and understanding of clouds and cloud feedbacks in CMIP5 models, CLIVAR Exchanges, 56, International CLIVAR Project Office, Southampton, U. K., 20–24.

Bower, K. N., S. J. Moss, D. W. Johnson, T. W. Choularton, J. Latham, P. R. A. Brown, A. M. Blyth, and J. Cardwell (1996), A parametrization of the ice water content observed in frontal and convective clouds, *Q. J. R. Meteorol. Soc.*, *122*, 1815–1844, doi:10.1002/qj.49712253605.

Cesana, G., and H. Chepfer (2012), How well do climate models simulate cloud vertical structure? A comparison between CALIPSO-GOCCP satellite observations and CMIP5 models, *Geophys. Res. Lett.*, *39*, L20803, doi:10.1029/2012GL053153.

Cesana, G., and H. Chepfer (2013), Evaluation of the cloud water phase in a climate model using CALIPSO-GOCCP, *J. Geophys. Res. Atmos*, *118*, 7922–7937, doi:10.1002/jgrd.50376.

Cesana, G., J. E. Kay, H. Chepfer, J. M. English, and G. deBoer (2012), Ubiquitous low-level liquid-containing Arctic clouds: New observations and climate model constraints from CALIPSO-GOCCP, *Geophys. Res. Lett.*, *39*, L20804, doi:10.1029/2012GL053385.

Chen, W.-T., C. P. Woods, J.-L. F. Li, D. E. Waliser, J.-D. Chern, W.-K. Tao, J. H. Jiang, and A. M. Tompkins (2011), Partitioning CloudSat ice water content for comparison with upper tropospheric ice in global atmospheric models, *J. Geophys. Res.*, *116*, D19206, doi:10.1029/2010JD015179.

Cheng, A., K.-M. Xu, Y. Hu, and S. Kato (2012), Impact of a cloud thermodynamic phase parameterization based on CALIPSO observations on climate simulation, *J. Geophys. Res.*, *117*, D09103, doi:10.1029/2011JD017263.

Chepfer, H., S. Bony, D. M. Winker, M. Chiriaco, J.-L. Dufresne, and G. Seze (2008), Use of CALIPSO lidar observations to evaluate the cloudiness simulated by a climate model, *Geophys. Res. Lett.*, *35*, L15704, doi:10.1029/2008GL034207.

Chepfer H., S. Bony, D. Winker, G. Cesana, J. L. Dufresne, P. Minnis, C. J. Stubenrauch, S. Zeng, (2010), The GCM Oriented Calipso Cloud Product (CALIPSO-GOCCP), *J. Geophys. Res.*, *115*, D00H16, doi:10.1029/2009JD012251.

Chepfer, H., G. Cesana, D. Winker, B. Getzewich, M. Vaughan, and Z. Liu (2013), Comparison of two different cloud climatologies derived from CALIOP Level 1 observations: The CALIPSO-ST and the CALIPSO-GOCCP, *J. Atmos. Oceanic Technol.*, *30*, 725–744, doi:10.1175/JTECH-D-12-00057.1.

Cober, S. G., A. I. George, A. V. Korolev, and J. W. Strapp (2001), Assessing cloud-phase conditions, *J. Appl. Meteorol.*, *40*(11), 1967–1983.

de Boer, G., E. W. Eloranta, and M. D. Shupe (2009), Arctic mixed-phase stratiform cloud properties from multiple years of surface-based measurements at two high-latitude locations, *J. Atmos. Sci.*, *66*(9), 2874–2887, doi:10.1175/2009JAS3029.1.

Dee, D. P., et al. (2011), The ERA-Interim reanalysis: Configuration and performance of the data assimilation system, *Q. J. R. Meteorol. Soc.*, *137*, 553–597, doi:10.1002/qj.828.

Deng, L., and X. Wu (2010), Effects of convective processes on GCM simulations of the Madden-Julian oscillation, *J. Clim.*, *23*, 352–377, doi:10.1175/2009JCLI3114.1.

Donner, L. J., et al. (2011), The dynamical core, physical parameterizations, and basic simulation characteristics of the atmospheric component AM3 of the GFDL global coupled model CM3, *J. Clim.*, *24*, 3484–3519, doi:10.1175/2011JCLI3955.1.

Doutriaux-Boucher, M., and J. Quaas (2004), Evaluation of cloud thermodynamic phase parametrizations in the LMDZ GCM by using POLDER satellite data, *Geophys. Res. Lett.*, *31*, L06126, doi:10.1029/2003GL019095.

Feigelson, E. M. (1978), Preliminary radiation model of a cloudy atmosphere: Part I—Structure of clouds and solar radiation, *Contrib. Atmos. Phys.*, *51*, 203–229.

Findeisen, W., (1938.), Die Kolloidmeteorologischen Vorgange bei der Niederschlasbildung (Collodial meteorological processes in the formation of precipitation), *Met. Z.*, *55*, 121.

Forbes, R. M., and M. Ahlgrimm (2014), On the representation of high-latitude boundary layer mixed-phase cloud in the ECMWF global model, *Mon. Weather Rev.*, *142*, 3425–3445, doi:10.1175/MWR-D-13-00325.1.

Gates, W. L. (1992), AMIP: The Atmospheric Model Intercomparison Project, *Bull. Am. Meteorol. Soc.*, *73*, 1962–1970, doi:10.1175/1520-0477(1992)073<1962:ATAMIP>2.0.CO;2.

Gregory, D., and D. Morris (1996), The sensitivity of climate simulations to the specification of mixed-phase clouds, *Clim. Dyn.*, *12*, 641–651.

Hogan, R. J., P. N. Francis, H. Flentje, A. J. Illingworth, M. Quante, and J. Pelon (2003), Characteristics of mixedphase clouds: I. Lidar, radar and aircraft observations from CLARE'98, *Q. J. R. Meteorol. Soc.*, *129*, 2089–2116.

Hourdin, F., et al. (2013), LMDZ5B: The atmospheric component of the IPSL climate model with revisited parameterizations for clouds and convection, *Clim. Dyn.*, *40*(9–10), 2193–2222, doi:10.1007/s00382-012-1343-y.

Hu, Y., S. Rodier, K. Xu, W. Sun, J. Huang, B. Lin, P. Zhai, and D. Josset (2010), Occurrence, liquid water content, and fraction of supercooled water clouds from combined CALIOP/IIR/MODIS measurements, *J. Geophys. Res.*, *115*, D00H34, doi:10.1029/2009JD012384.

Huffman, G. J., R. F. Adler, M. Morrissey, D. T. Bolvin, S. Curtis, R. Joyce, B. McGavock, and J. Susskind (2001), Global precipitation at one-degree daily resolution from multi-satellite observations, *J. Hydrometeorol.*, *2*, 36–50.

Huffman, G. J., D. T. Bolvin, E. J. Nelkin, D. B. Wolff, R. F. Adler, G. Gu, Y. Hong, K. P. Bowman, and E. F. Stocker (2007), The TRMM Multisatellite Precipitation Analysis (TMPA): Quasi-global, multiyear, combined-sensor precipitation estimates at fine scales, *J. Hydrometeorol.*, *8*, 38–55.

Jiang, X., et al. (2015), Vertical structure and physical processes of the Madden-Julian oscillation: Exploring key model physics in climate simulations, *J. Geophys. Res. Atmos.*, *120*, 4718–4748, doi:10.1002/2014JD022375.

Kiehl, J. T., and K. E. Trenberth (1997), Earth's annual global mean energy budget, *Bull. Am. Meteorol. Soc.*, *78*, 197–208.

King, M. D., S. Platnick, W. Paul Menzel, S. A. Ackerman, and P. A. Hubanks (2013), Spatial and temporal distribution of clouds observed by MODIS onboard the terra and aqua satellites, *IEEE Trans. Geosci. Remote Sens.*, *51*, 3826–3852, doi:10.1109/TGRS.2012.2227333.

Klein, S. A., and C. Jakob (1999), Validation and sensitivities of frontal clouds simulated by the ECMWF model, *Mon. Weather Rev.*, *127*(10), 2514–2531, doi:10.1175/1520-0493(1999)127<2514:VASOFC>2.0.CO;2.

Komurcu, M., T. Storelvmo, I. Tan, U. Lohmann, Y. Yun, J. E. Penner, Y. Wang, X. Liu, and T. Takemura (2014), Intercomparison of the cloud water phase among global climate models, *J. Geophys. Res. Atmos.*, *119*, 3372–3400, doi:10.1002/2013JD021119.

Korolev, A. V., G. A. Isaac, S. G. Cober, J. W. Strapp, and J. Hallett (2003), Microphysical characterization of mixed-phase clouds, *Q. J. R. Meteorol. Soc.*, *129*, 39–65, doi:10.1256/qj.01.204.

Li, J.-L. F., D. E. Waliser, W.-T. Chen, B. Guan, T. Kubar, G. Stephens, H.-Y. Ma, M. Deng, L. Donner, C. Seman, and L. Horowitz (2012), An observationally based evaluation of cloud ice water in CMIP3 and CMIP5 GCMs and contemporary reanalyses using contemporary satellite data, *J. Geophys. Res.*, *117*, D16105, doi:10.1029/2012JD017640.

Li, Z.-X., and H. Le Treut (1992), Cloud-radiation feedbacks in a general circulation model and their dependence on cloud modelling assumptions, *Clim. Dyn.*, *7*, 133–139.

Liu, G., and J. A. Curry (1996), Large-scale cloud features during January 1993 in the North Atlantic Ocean as determined from SSM/I and SSM/T2 observations, *J. Geophys. Res.*, *101*, 7019–7032, doi:10.1029/95JD03859.

Liu, X., et al. (2011), Testing cloud microphysics parameterizations in NCAR CAM5 with ISDAC and M-PACE observations, *J. Geophys. Res.*, *116*, D00T11, doi:10.1029/2011JD015889.

Lohmann, U., and E. Roeckner (1996), Design and performance of a new cloud microphysics scheme developed for the ECHAM general circulation model, *Clim. Dyn.*, *12*(8), 557–572.

Marchand, R. T., J. Haynes, G. G. Mace, T. Ackerman, G. Stephens, (2009), A comparison of simulated cloud radar output from the multiscalemodeling framework global climate model with CloudSat cloud radar observations, *J. Geophys. Res.*, *114*, D00A20, doi:10.1029/2008JD009790.

Martin, G. M., et al. (2011), The HadGEM2 family of met office unified model climate configurations, *Geosci. Model Dev.*, *4*(3), 723–757, doi:10.5194/gmd-4-723-2011.

Molod, A., L. Takacs, M. Suarez, J. Bacmeister, I.-S. Song, and A. Eichmann (2012), The GEOS-5 atmospheric general circulation model: Mean climate and development from MERRA to Fortuna, NASA Tech. Memorandum 104606 Volume 28, NASA, Goddard Space Flight Center, Greenbelt, Md.

Naud, C. M., A. D. Del Genio, M. Haeffelin, Y. Morille, V. Noel, J.-C. Dupont, D. D. Turner, C. Lo, and J. Comstock (2010), Thermodynamic phase profiles of optically thin midlatitude clouds and their relation to temperature, *J. Geophys. Res.*, *115*, D11202, doi:10.1029/2009JD012889.

Neale, R. B., et al. (2010a), Description of the NCAR Community Atmosphere Model (CAM 4.0), *NCAR Tech. Note NCAR/TN-XXX+STR,* 206 pp., Natl. Cent. for Atmos. Res., Boulder, Colo.

Neale, R. B., et al. (2010b), Description of the NCAR Community Atmosphere Model (CAM 5.0), *NCAR Tech. Note NCAR/TN-XXX+STR*, 282 pp., Natl. Cent. for Atmos. Res, Boulder, Colo.

Petch, J., D. Waliser, X. Jiang, P. K. Xavier, and S. Woolnough (2011), A global model intercomparison of the physical processes associated with the Madden-Julian Oscillation, GEWEX News, 5 pp., Aug.

Pincus, R., S. Platnick, S. A. Ackerman, R. S. Hemler, and R. J. P. Hofmann (2012), Reconciling simulated and observed views of clouds: MODIS, ISCCP, and the limits of instrument simulators, *J. Clim.*, *25*, 4699–4720, doi:10.1175/JCLI-D-11-00267.1.

Pruppacher, H. R., and J. D. Klett (1997), *Microphysics of Clouds and Precipitation*, 2nd ed., 954 pp., Kluwer Acad., Dordrecht, Netherlands.

Rienecker, M. M., et al. (2011), MERRA: NASA's Modern-Era Retrospective Analysis for Research and Applications, *J. Clim.*, *24*, 3624–3648, doi:10.1175/JCLI-D-11-00015.1.

Rogers, R. R., and M. K. Yau (1989), *A Short Course in Cloud Physics*, 3rd ed., Butterworth-Heinemann, Burlington, Mass.

Schmidt, G. A., et al. (2006), Present-day atmospheric simulations using GISS ModelE: Comparison to in situ, satellite, and reanalysis data, *J. Clim.*, *19*, 153–192, doi:10.1175/JCLI3612.1.

Shupe, M. D. (2011), Clouds at Arctic Atmospheric Observatories: Part II. Thermodynamic phase characteristics, *J. Appl. Meteorol. Climatol.*, *50*, 645–661, doi:10.1175/2010JAMC2468.1.

Shupe, M. D., and J. M. Intrieri (2004), Cloud radiative forcing of the Arctic surface: The influence of cloud properties, surface albedo, and solar zenith angle, *J. Clim.*, *17*, 616–628.

Smith, R. N. B. (1990), A scheme for predicting layer clouds and their water content in a general circulation model, *Q. J. R. Meteorol. Soc.*, *116*, 435–460, doi:10.1002/qj.49711649210.

Sonntag, D. (1990), Important new values of the physical constants of 1986, vapour pressure formulations based on the ITS-90, and psychrometer formulae, *Z. Meteorol.*, *40*, 340–344.

Stephens, G. L., and C. D. Kummerow (2007), The remote sensing of clouds and precipitation from space: A review, *J. Atmos. Sci.*, *64*, 3742–3765, doi:10.1175/2006JAS2375.1.

Stevens, B., et al. (2013), Atmospheric component of the MPI-M Earth System Model: ECHAM6, *J. Adv. Model. Earth Syst.*, *5*, 146–172, doi:10.1002/jame.20015.

Stocker, T. F., et al. (2013), *Intergovernmental Panel on Climate Change (IPCC), Climate Change 2013: The Physical Science Basis, Contribution of Working Group I to the Fifth Assessment Report of the Intergovernmental Panel on Climate Change*, Cambridge Univ. Press, Cambridge, U. K.

Stubenrauch, C. J., et al. (2013), Assessment of global cloud datasets from satellites: Project and database initiated by the GEWEX radiation panel, *Bull. Am. Meteorol. Soc.*, *94*, 1031–1049, doi:10.1175/BAMS-D-12-00117.1.

Sun, Z., and K. P. Shine (1994), Studies of the radiative properties of ice and mixed-phase clouds, *Q. J. R. Meteorol. Soc.*, *120*, 111–137, doi:10.1002/qj.49712051508.

Takemura, T., T. Nozawa, S. Emori, T. Y. Nakajima, and T. Nakajima (2005), Simulation of climate response to aerosol direct and indirect effects with aerosol transport-radiation model, *J. Geophys. Res.*, *110*, D02202, doi:10.1029/2004JD005029.

Tao, W.-K. (2003), Goddard Cumulus Ensemble (GCE) model: Application for understanding precipitation processes, in *Cloud Systems, Hurricanes, and the Tropical Rainfall Measuring Mission (TRMM)—A Tribute to Dr. Joanne Simpson*, *Meteorol. Monogr. Ser.*, vol. 29, pp. 107–138, Am. Meteorol. Soc., Boston, Mass.

Tao, W.-K., and J. Simpson (1993), The Goddard cumulus model ensemble model: Part I. Model description, *Terr. Atmos. Oceanic. Sci.*, *4*, 35–72.

Taylor, K. E., R. J. Stouffer, and G. A. Meehl (2012), An Overview of CMIP5 and the experiment design, *Bull. Am. Meteorol. Soc.*, *93*, 485–498, doi:10.1175/BAMS-D-11-00094.1.

Tiedtke, M. (1993), Representation of clouds in large-scale models, *Mon. Weather Rev.*, *121*, 3040–3061.

Tonttila, J., P. Räisänen, and H. Järvinen (2013), Monte Carlo-based subgrid parameterization of vertical velocity and stratiform cloud microphysics in ECHAM5.5-HAM2, *Atmos. Chem. Phys.*, *13*, 7551–7565, doi:10.5194/acp-13-7551-2013.

Tsuang, B. J., C. Y. Tu, J. L. Tsai, J. A. Dracup, K. Arpe, and T. Meyers (2009), A more accurate scheme for calculating Earth's skin temperature, *Clim. Dyn.*, *32*, 251–272.

Tsushima, Y., S. Emori, T. Ogura, M. Kimoto, M. J. Webb, K. D. Williams, M. A. Ringer, B. J. Soden, B. Li, and N. Andronova (2006), Importance of the mixed-phase cloud distribution in the control climate for assessing the response of clouds to carbon dioxide increase: A multi-model study, *Clim. Dyn.*, *27*(2–3), 113–126.

Voldoire, A., et al. (2011), The CNRM-CM5.1 global climate model: Description and basic evaluation, *Clim. Dyn.*, *40*, 2091–2121, doi:10.1007/s00382-011-1259-y.

von Salzen, K., et al. (2013), The Canadian fourth generation atmospheric global climate model (CanAM4): Part I. Representation of physical processes, *Atmos. Ocean*, doi:10.1080/07055900.2012.755610.

Waliser, D. E., et al. (2009), Cloud ice: A climate model challenge with signs and expectations of progress, *J. Geophys. Res.*, *114*, D00A21, doi:10.1029/2008JD01001.

Wallace, J. M., and P. V. Hobbs (2006), *Atmospheric Science an Introduction Survey*, 504 pp., Academic Press, San Diego, Calif..

Watanabe, M. (2010), Improved climate simulation by MIROC5: Mean states, variability, and climate sensitivity, *J. Clim.*, *23*, 6312–6335.

West, R. E. L., P. Stier, A. Jones, C. E. Johnson, G. W. Mann, N. Bellouin, D. G. Partridge, and Z. Kipling (2014), The importance of vertical velocity variability for estimates of the indirect aerosol effects, *Atmos. Chem. Phys.*, *14*, 6369–6393, doi:10.5194/acp-14-6369-2014.

Wielicki, B. A., et al. (1996), Clouds and the Earth's Radiant Energy System (CERES): An earth observing system experiment, *Bull. Am. Meteorol. Soc.*, *77*, 853–868.

Winker, D. M., et al. (2010), The CALIPSO Mission: A Global 3D View of Aerosols and Clouds, *Bull. Am. Meteorol. Soc.*, *91*, 1211–1229, doi:10.1175/2010BAMS3009.1.

Wu, T., R. Yu, F. Zhang, Z. Wang, M. Dong, L. Wang, X. Jin, D. Chen, and L. Li (2010), The Beijing climate center for atmospheric general circulation model (BCC-AGCM2.0.1): Description and its performance for the present-day climate, *Clim. Dyn.*, *34*, 123–147, doi:10.1007/s00382-009-0594-8.

Wyant, M. C., C. S. Bretherton, J. T. Bacmeister, J. T. Kiehl, I. M. Held, M. Zhao, S. A. Klein, and B. J. Soden (2006), A comparison of low-latitude cloud properties and their response to climate change in three AGCMs sorted into regimes using mid-tropospheric vertical velocity, *Clim. Dyn.*, *27*, 261–279.

Yukimoto, S., et al. (2012), A new Global Climate Model of the Meteorological Research Institute: MRI-CGCM3—Model description and basic performance, *J. Meterol. Soc. Jpn.*, *90A*, 23–64, doi:10.2151/jmsj.2012-A02.

Zuidema, P., B. Baker, Y. Han, J. Intrieri, J. Key, P. Lawson, S. Matrosov, M. Shupe, R. Stone, and T. Uttal (2005), An Arctic springtime mixed-phase cloudy boundary layer observed during SHEBA, *J. Atmos. Sci.*, *62*(1), 160–176.